Available online at www.sciencedirect.com

SciVerse ScienceDirect

Geochimica et Cosmochimica Acta 79 (2012) 1–19

Geochimica et Cosmochimica Acta

www.elsevier.com/locate/gca

Experimental investigation of the influence of oxygen fugacity on the source depths for high titanium lunar ultramafic magmas

Michael J. Krawczynski *, Timothy L. Grove

MIT, 77 Massachusetts Avenue, Cambridge, MA 02139, USA

Received 31 January 2011; accepted in revised form 27 October 2011; available online 15 November 2011

Abstract

High pressure and high temperature experiments were carried out on two pristine ultramafic high titanium glass compositions from the Moon. The investigated compositions are the Apollo 15 red glass (13.8 wt% TiO_2) and Apollo 17 orange glass (9.1 wt% TiO_2). Temperatures spanned the range of 1320–1570 °C, and pressures 0.8–3.3 GPa. Graphite and iron metal capsules were used to control f_{O_2} at iron–wüstite (ΔIW) + 1.3 log units to ΔIW−2.1, respectively. Multiple saturation with olivine and orthopyroxene on the liquidus occurs at 1.2 GPa and 1350 °C for the red glass, and 2.5 GPa and 1530 °C for the orange glass in graphite capsules. In Fe capsules the multiple saturation points (MSP) shift to higher pressure, and are 2.2 GPa and 1450 °C for the red glass, and 3.1 GPa and 1560 °C for the orange glass. The magnitude of the shift in MSP increases with increasing TiO_2 content. The changes in MSP are caused by f_{O_2} and correspond to a ~200 km shift in the estimated minimum depth of origin for the red glass, and up to a 300 km range in depth between the red and orange glass depth of origin. Using independent estimates of f_{O_2} for the orange glass source region of ΔIW−0.6 (Sato, 1979; Nicholis and Rutherford, 2009), interpolation of our phase stability data yields a pressure of multiple saturation of 2.8 GPa. Our results confirm that the red and orange glasses are buoyant with respect to model lunar interior assemblages at their multiple saturation pressures. The difference in the pressure of liquidus multi-phase saturation is possibly due to a shift in the Ti–Fe coordination in high-Ti melts. Evidence for this coordination change comes from systematic changes in olivine–melt Fe–Mg K_D's with f_{O_2}, pressure, temperature, and TiO_2 content.

1. INTRODUCTION

The lunar high-titanium ultramafic glasses are among the most unusual volcanic rocks found in the solar system, spanning a range of TiO_2 values from 9 to 16 wt% TiO_2 (Fig. 1, Delano, 1986). The ultramafic glasses are believed to be the products of high-degree remelting of Ti-rich cumulates that are a product of extreme chemical differentiation of a global magma ocean that solidified early in lunar history (Solomon and Longhi, 1977; Warren, 1985; Snyder et al., 1992). Experimental studies of these glasses, together with the high-Ti mare basalt suite, are a prerequisite for understanding the nature of their melting processes, source materials, and depth of origin in the lunar mantle. Experimental studies are also important to further explore the effects that high-Ti contents have on silicate melt structure (Mysen and Neuville, 1995). As demonstrated originally by Longhi et al. (1978), high-Ti melts have a significant influence on Fe–Mg partitioning between olivine and melt.

This paper presents new experimental data on the high-pressure, high-temperature phase relations of two high-Ti ultramafic glasses, the Apollo 15 red (A15R, 13.8 wt% TiO_2) and the Apollo 17 orange (A17O, 9 wt% TiO_2) glasses, over a range of Moon-relevant oxygen fugacities (f_{O_2}). We find that variation in f_{O_2} has significant effects on the high pressure phase equilibria. Assuming that these magmas come from a polymineralic source region in the

* Corresponding author. Current address: Case Western Reserve University, Cleveland, OH 44120, USA. Tel.: +1 617 253 2876.

E-mail addresses: mjk181@case.edu (M.J. Krawczynski), tlgrove@mit.edu (T.L. Grove).

0016-7037/$ - see front matter © 2011 Elsevier Ltd. All rights reserved.
doi:10.1016/j.gca.2011.10.043

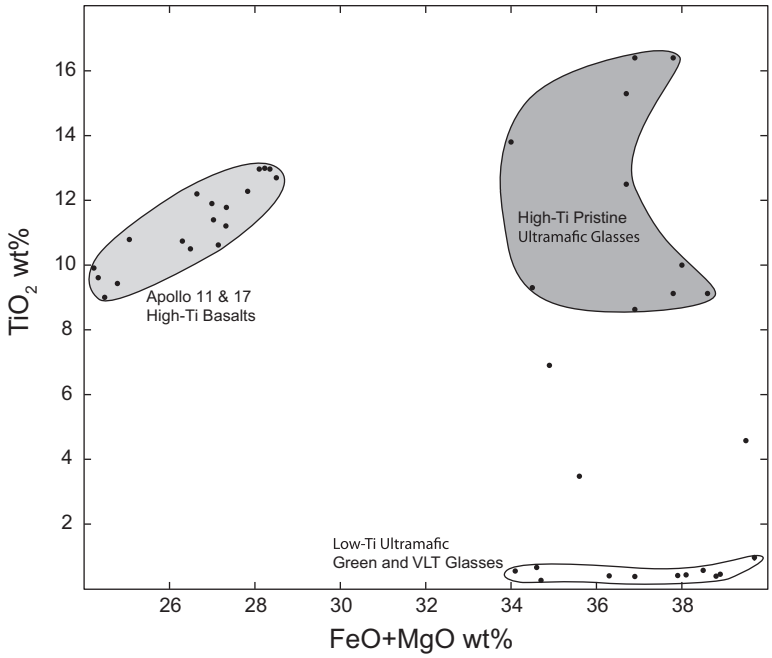

Fig. 1. Compositional variations between the ultramafic picritic glass suites and the high-Ti basalts of Apollo 11 and 17. Data are from Papike et al. (1998).

lunar mantle, we use our experimental results to infer the pressure and temperature of melt generation based on co-saturation of olivine and orthopyroxene as liquidus phases, which is referred to as the multiple saturation point (MSP).

Previous experimental studies on high-Ti magmas have been carried out on a variety of compositions. Dickinson and Hess (1985) and Gaetani et al. (2008) used synthetic analog liquids to determine the saturation of rutile in a range of silicate liquids. Xirouchakis et al. (2001) and Longhi et al. (1978) explored the effect of TiO_2 on major element partitioning between olivine and liquid. Longhi et al. (1972) performed high-pressure experiments on Apollo 17 mare basalts and Green et al. (1975), Delano (1980), Wagner and Grove (1997) carried out phase equilibrium studies on the Apollo 17 orange, Apollo 15 red, and Apollo 14 black glasses, respectively. However, all of the previous studies were conducted in different labs and with different experimental procedures that may impose different oxygen fugacities on the experimental sample. In this study we show that phase equilibria as well as mineral–melt element partitioning are functions of oxygen fugacity in these high-titanium silicate melts.

2. EXPERIMENTS AND ANALYTICAL METHODS

2.1. Starting materials

The compositions of the A15R and A17O glasses were created by mixing high purity reagent grade oxides and silicates, MgO, $CaSiO_3$, Fe_2O_3, Cr_2O_3, Al_2O_3, MnO, Na_2SiO_3, SiO_2. Fe-metal sponge and Fe_2O_3 were added in proportion to obtain an overall stoichiometry of FeO. The oxides were mixed under ethanol in an automatic agate mortar for 3 h. Fe-metal sponge was then added to the mixture and ground for an additional 1 h. The ground starting material was then conditioned at 1-atm pressure in a Deltech furnace for 24 h at f_{O_2} conditions close to IW at 1000 °C under a flow of CO_2 and H_2 gas. The conditioned powder was then reground dry in an agate mortar by hand. The composition of the starting material has been verified by analyzing the products of liquid-only high pressure experiments, and closely matches the compositions of Delano (1986) (Table 1).

2.2. Experimental techniques

Experiments were performed in the Massachusetts Institute of Technology experimental petrology laboratory in a 0.5″ piston cylinder apparatus (Boyd and England, 1960). The ground, conditioned starting material was packed into either graphite or spec-pure Fe capsules and dried at 120 °C for between 24 h and 4 weeks prior to running an experiment. Experiments on the A15R composition in graphite capsules were placed into an outer Pt jacket that was welded shut. To eliminate the possibility of Fe loss to the outer Pt jacket, we switched to graphite-only capsules for experiments on the A17O composition. The piston cylinder pressure cell assembly and experimental procedure is the same as that described in Wagner and Grove (1997).

Piston cylinder experiments on the A15R and A17O compositions were performed from 0.8 to 3.3 GPa and 1320–1570 °C. Pressure was calibrated using the breakdown of Ca-Tschermak pyroxene to ghelenite + corundum + anorthite (Hays, 1966), and the spinel to garnet transition in the CMAS system (Longhi, 2005). It was found that no friction correction to experiment pressure was necessary. Experiments used a W–Re thermocouple

Table 1
Synthetic starting materials and natural compositions.[a]

Composition	SiO_2	TiO_2	Al_2O_3	Cr_2O_3	FeO	MnO	MgO	CaO	Na_2O	K_2O	Total
Natural A15R	35.6	13.8	7.15	0.77	21.9	0.25	12.1	7.89	0.49	0.12	100.07
Synthetic A15R	35.8	13.5	7.11	0.74	22.0	0.24	12.5	7.74	0.31	–	99.94
Natural A17O	38.5	9.12	5.79	0.69	22.9	–	14.9	7.40	0.38	–	99.68
Synthetic A17O	38.9	8.78	5.81	0.67	22.3	0.27	15.7	7.37	0.26	–	99.95

[a] Natural compositions are from Delano (1986) and synthetic materials are an average of the glass compositions from experiments that were super-liquidus (C333, C346, C315 for A15O; D195, C397, and C409 for A17O).

and no correction was applied for a pressure effect on thermocouple emf. Temperature was controlled to within ±2 °C on the Eurotherm controller, and the temperature is accurate to ±5 °C.

Experimental durations varied from 4.5 to 46 h. Experimental conditions are reported in Tables 2 and 3. The durations of experiments are significantly longer than previous studies on these two lunar compositions (Green et al., 1975; Delano, 1980), and the extended times ensured as close an approach to equilibrium as possible. Fig. 2c and d shows typical experiment results for Fe-metal and graphite capsule experiments.

In order to obtain glass that did not form quench crystals during cooling of the experiment we used a pressure-quenching technique where the piston load was released at the same moment the power was shut off to the experiment (Putirka et al., 1996). Thus the experiment is slightly superheated while the liquid is cooling below the glass transition temperature.

2.3. Analytical methods

Experimental run products were analyzed by electron microprobe on the JEOL 733 Superprobe at MIT. Beam conditions were 15 kV accelerating voltage and a 10 nA current. All glass analyses were done with a 10 μm diameter beam, and all mineral phases were analyzed with a focused 1–2 μm beam (with the exception of decomposed garnets). The CITZAF correction procedure of Armstrong (1995) was used for data reduction. A materials balance calculation was used to estimate phase proportions and to determine whether FeO had been gained or lost from the experimental charge through reaction with the sample capsule. Results of these calculations are reported in Tables 2 and 3. Major and minor element concentrations in all the phases are reported in Tables 4 and 5. Errors reported are the 1-σ standard deviation of the arithmetic mean of replicate analyses on each phase.

3. EXPERIMENTAL RESULTS

3.1. Control of f_{O_2}

A series of experiments was devised to estimate the variations in f_{O_2} imposed by graphite and Fe capsules by adding a small f_{O_2} sensor to the capsule + starting material. These f_{O_2} sensor experiments were run in both graphite and Fe capsules and used metal–alloy equilibria to determine the oxygen fugacity imposed by each capsule type. Several investigators have inferred the f_{O_2} imposed by graphite sample containers in piston cylinder experiments (Ulmer and Luth, 1991; Holloway et al., 1992; Yasuda and Fujii, 1993; Medard et al., 2008). The results of Medard et al. (2008) suggest that the graphite capsule assembly imposes an upper limit of ΔIW+2 (where ΔIW±x is the value of f_{O_2} relative to the IW buffer in $\log_{10}$ units at the given temperature), however starting materials that were more reduced than the upper limit could maintain their lower f_{O_2}.

The f_{O_2} in the graphite capsule experiments was measured independently by the equilibrium between coexisting Cr-rich spinel, olivine, opx, and melt as well as by an experiment with a small bead of FePt metal. The FePt alloy was placed in a graphite capsule and allowed to equilibrate with the IW-conditioned melt and graphite capsule assembly at 1.7 GPa and 1420 °C for 24 h. The composition of this re-equilibrated alloy and the method of Grove (1981) were used to determine a f_{O_2} of ΔIW+1.5 (Table 4 and Fig. 2a). For an experiment that was saturated with olivine, opx, and spinel at 1.1 GPa and 1320 °C (C318, 22.6 h duration), the f_{O_2} was determined using the oxybarometer of Ballhaus et al. (1991a,b). The oxygen fugacity obtained was ΔIW+1.25. These methods agreed to within 0.25 log units. Both methods yield f_{O_2} values higher than the IW conditioning of the starting material, but are within the expected f_{O_2} range determined for graphite capsules (Ulmer and Luth, 1991; Holloway et al., 1992; Yasuda and Fujii, 1993; Medard et al., 2008).

Little experimental work has been done to obtain a quantitative estimate of the f_{O_2} imposed by Fe capsules used in piston cylinder experiments. Experiments in Fe-metal capsules are saturated with metallic Fe, but undersaturated with respect to wüstite, thus the activity of FeO is less than unity. The saturation with metal and less than unity activity of FeO ensures the f_{O_2} of the experiment to be below the IW buffer, but the absolute value needs to be determined. To measure the f_{O_2} imposed by the Fe-metal capsule, we devised an f_{O_2} sensor experiment using FeCr alloys to record f_{O_2}. We placed a layer of Cr_2O_3 (eskolaite) powder at the bottom of a spec-pure Fe-metal capsule and inserted an Fe foil cup that contained the A15R starting material. The assembly was then run at 1.3 GPa and 1420 °C for 92 h. The Fe foil disaggregated during the experiment into discrete FeCr alloy blebs (Fig. 2b). The composition of these blebs was analyzed in electron microprobe line transects across the diameter of the bleb. If a constant Cr content was observed, the bleb was assumed to have reached equilibrium, and this value of X_{Cr}^{FeCr}

Table 2
Run conditions and products for A15R starting material.

Run	Capsule	T (°C)	GPa	Time (h)	Phases (calculated mode)[a]	Olv K_D[b]	Opx K_D	Cpx K_D	Ilm K_D	Gt/Sp K_D	% FeO loss/gain
C321	Fe	1410	2	6.8	olv(2) + opx(4) + liq(93)	0.270	0.252				1.3
C322	Fe	1440	2.3	16.2	olv(1) + opx(6) + liq(93)	0.274	0.246				0.8
C323	Fe	1410	2.3	24.2	olv(3) + opx(3) + cpx(16) + gnt(3) + liq(75)	0.240	0.239			0.396	2.1
C324	Fe	1380	1.7	24	olv(3) + opx(7) + liq(89)	0.262	0.252				3.8
C326	Fe	1410	1.7	18.2	olv(6) + opx(3) + liq(90)	0.261	0.241				2.3
C329	Fe	1440	2	18	olv(1) + opx(3) + liq(96)	0.264	0.250				2.6
C333	Fe	1470	2	7.0	liq						9.0
C346	Fe	1440	1.7	19.3	liq						−0.8
B1058	Fe	1420	1.3	91.8	sp + esk + FeCr + liq						
C361	C	1420	1.7	24	olv + sp + PtFe + liq						
B1025	C + Pt	1350	0.8	4.6	olv + sp + liq	0.258					
B1027	C + Pt	1320	0.8	4.7	olv(19) + opx(−14) + sp(?) + liq(94)	0.235	0.274				−0.1
C309	C + Pt	1350	1.95	14	opx(27) + cpx(−22) + sp(1) + ilm(−7) + liq(100)		0.278	0.315	1.87	1.42	−1.7
C310	C + Pt	1320	1.7	21.5	opx(28) + cpx(−20) + sp(<1) + ilm(−6) + liq(98)		0.269	0.297	1.73	1.18	−2.1
C311	C + Pt	1380	2	19.8	opx(6) + sp(2) + liq(93)		0.310			1.54	−11.3
C312	C + Pt	1350	1.7	19.4	opx(7) + sp(2) + liq(93)		0.314			1.63	−8.1
C313	C + Pt	1410	2	15.5	opx(−3) + sp(1) + liq(103)		0.333			1.38	−7.5
C314	C + Pt	1380	1.7	15.1	opx(1) + sp(4) + liq(96)		0.276			1.37	−10.5
C315	C + Pt	1440	2	7.9	liq						−7.6
C316	C + Pt	1400	1.7	8.3	sp(2) + liq(98)					1.30	−5.5
C317	C + Pt	1350	1.4	21.4	opx(4) + sp(3) + liq(94)		0.250			1.30	−5.6
C318	C + Pt	1320	1.1	22.6	olv(10) + opx(−6) + sp(3) + liq(94)	0.263	0.256			1.37	−5.4
C319	C + Pt	1380	1.4	9.7	sp + liq						
C320	C + Pt	1350	1.1	7	olv(1) + sp(3) + liq(97)	0.271				1.41	−2.9
C332	C + Pt	1320	1.4	46.3	olv(4) + opx(13) + sp(2) + ilm(1) + liq(81)	0.249	0.227		1.35	1.34	−0.4
C338	C + Pt	1365	1.25	24	sp + liq						

(?) No sp observed in this experiment, but the mass balance has a Cr deficit and the position on the phase diagram suggests there should be a small amount of it. *Abbreviations:* olv = olivine, opx = orthopyroxene, cpx = clinopyroxene, sp = spinel, gt = garnet, ilm = ilmenite, esk = eskolaite, liq = quenched melt.

[a] Negative modes indicate a failure of the linear regression analysis.

[b] K_D is the Fe–Mg mineral–melt exchange coefficient.

Table 3
Run conditions and products for A17O starting material.

Run #	Capsule	T (°C)	GPa	Time (h)	Phases	Olv K_D	Opx K_D	Cpx K_D	Gt/Sp K_D	% FeO loss/gain
D176	Fe	1550	3.1	18.1	olv(10) + opx(−11) + liq(103)	0.282	0.300			−7.5
D187	Fe	1510	3.32	45.3	olv(9) + cpx(26) + gnt(11) + liq(55)	0.249		0.259	0.478	−2.3
D190	Fe	1550	3.15	23.1	olv(7) + opx(2) + cpx(7) + liq(84)	0.271	0.269	0.297		−2.2
C408	Fe	1535	2.85	19.8	olv(8) + liq(90)	0.283				21.4
D195	Fe	1570	3.15	10.5	liq(100)					−5.2
D198	Fe	1550	3.3	6.5	olv(5) + opx(18) + cpx(−13) + liq(90)	0.282	0.278	0.295		−1.9
D199	Fe	1570	3.31	7.4	olv(4) + opx(−2) + liq(98)	0.294	0.268			−1.4
D233	Fe	1550	2.9	6	olv + liq					
B1050	C	1390	1.3	17.1	olv(8) + liq(91)	0.276				−1.5
C363	C	1380	1.5	6.7	olv(12) + opx(10) + sp(1) + liq(77)	0.278	0.239		1.35	0.5
C364	C	1360	1.3	13.4	olv(15) + opx(6) + sp(1) + liq(79)	0.281	0.243		1.41	0
C365	C	1340	1.3	8.8	olv(16) + opx(6) + sp(1) + liq(78)	0.292	0.247		1.48	0.4
C366	C	1420	1.7	15.8	olv + sp + liq	0.301				
C367	C	1405	1.5	22.5	olv(7) + sp(2) + liq(92)	0.348			1.61	−6.1
C368	C	1410	1.3	21.7	olv(10) + sp(1) + liq(89)	0.293			1.49	−1.6
C370	C	1420	1.6	12.6	olv(12) + opx(−4) + sp(<1) + liq(92)	0.296	0.263		1.41	0.1
C371	C	1430	1.9	26.2	olv(9) + opx(3) + liq(88)	0.289	0.253			0.2
C373	C	1440	2.15	9.1	olv(8) + opx(14) + sp(<1) + liq(77)	0.256	0.225		1.09	0.9
C376	C	1460	2.15	19.7	olv(5) + opx(8) + liq(86)	0.289	0.249			0.6
C380	C	1470	1.9	21.9	olv(2) + liq(98)	0.332				−4.4
C381	C	1480	2.1	19.7	olv(4) + liq(96)	0.324				−4.6
C382	C	1450	1.9	24.9	olv(9) + liq(91)	0.302				−2.3
C388	C	1490	2.3	23	olv(7) + opx(−1) + liq(94)	0.280	0.252			−0.2
C389	C	1510	2.3	20.7	olv(4) + liq(96)	0.298				−3.7
C395	C	1540	2.5	8	olv(2) + opx(−1) + liq(100)	0.317	0.284			−1.9
C396	C	1520	2.5	26.8	olv(6) + opx(−12) + liq(107)	0.354	0.313			−2.5
C397	C	1560	2.5	8.7	liq(100)					0.6
C409	C	1555	2.7	14.3	liq(100)					−4.5

See Table 2 for explanations of abbreviations.

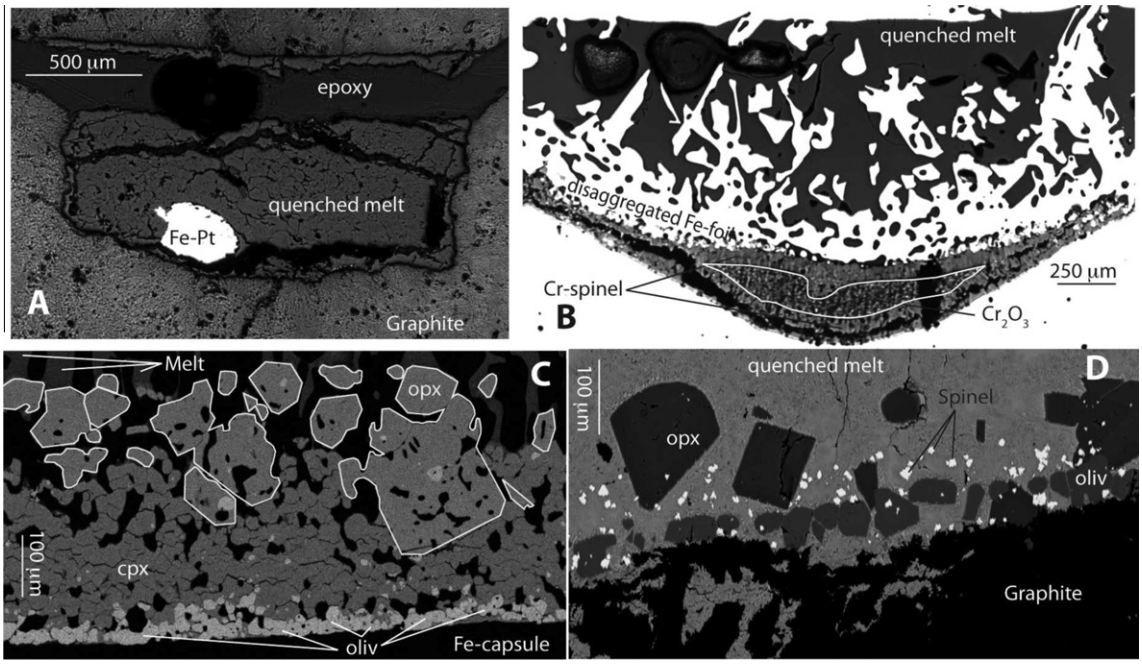

Fig. 2. (A) Reflected light photomicrograph of a graphite capsule f_{O_2} sensor experiment. The experiment was ground away until a good exposure of the FePt bead was obtained. (B) Reflected light photomicrograph of the Fe capsule f_{O_2} sensor experiment. The small disaggregated beads of FeCr were analyzed for their Cr content to determine the f_{O_2}. (C) Mg X-ray intensity map of experiment D190. Visible are the phases: melt, olivine, cpx, and opx. The black areas are the Fe-capsule (no Mg). (D) Electron backscatter image of experiment C318. This experiment contains melt, olivine, opx, and spinel.

(0.0309) was used in the following calculation. The equilibrium constant is defined by the equation:

$$\ln K = \frac{(a_{Cr}^{FeCr})^2 (f_{O_2})^{\frac{3}{2}}}{a_{Cr_2O_3}^{esk}} \quad (1)$$

where a_m^n is the activity of the m component in phase n and f_{O_2} is the oxygen fugacity. The non-ideality in the FeCr binary system can be represented with a Margules-parameter expansion:

$$RT\ln(\gamma_{Cr}^{FeCr}) = \left[W_{CrFe} + 2(W_{CrFe} - W_{FeCr})X_{Cr}^{FeCr}\right](X_{Fe}^{FeCr})^2 \quad (2)$$

where γ_{Cr}^{FeCr} is the activity coefficient of Cr-metal in the FeCr alloy, and X_m^n is the mole fraction of component m in phase n. Using the values of W_{CrFe} and W_{FeCr} from Kessel et al. (2003), and the presence of pure Cr_2O_3 eskolaite to set the activity at 1, Eq. (1) can be solved for oxygen fugacity. For our experiment the f_{O_2} was calculated to be $\Delta IW - 2.1$. Thus the Fe-metal capsule does not preserve the f_{O_2} conditioning of the starting material, and the two capsules types produce a greater than three log-unit spread of oxygen fugacity. The f_{O_2} of the orange glass falls between these values at $\Delta IW - 0.6$ (Sato, 1979; Weitz et al., 1997; Nicholis and Rutherford, 2009) and thus is bracketed by these experiments.

3.2. Approach to equilibrium

To demonstrate that the experimental durations were sufficient to reach equilibrium, we used the common approach of calculating mineral–liquid Fe–Mg exchange coefficients (K_D^{Fe-Mg}, Tables 2 and 3). We find that the K_D^{Fe-Mg} value is not constant, but varies systematically with pressure, temperature, and f_{O_2} and is consistent with previous long-duration experimental studies of high-Ti liquids (Wagner and Grove, 1997; Xirouchakis et al., 2001).

In addition to the checks on the equilibrium partitioning of Fe–Mg, the phase compositions were used in a least squares multiple linear regression analysis to determine Fe loss/gain. The Fe loss/gain was less than ±6% for 85% of the experiments reported here. For low crystallinity, near-liquidus experiments, the least squares multiple linear regression analysis captures the mineral modes accurately. The multiple linear regression technique is not as successful for highly crystalline experiments as evidenced by large negative coefficients for some of the minerals (Tables 2 and 3). The negative coefficients occur because the inversion technique is unable to distinguish between solutions to the system of equations with positive coefficients and unrealistic negative ones. This occurs when multiple solutions are equally good (or bad) fits to the data (Press et al., 1986). However, even in experiments where the linear regression method fails, the K_D^{Fe-Mg} values for the silicates and oxides are similar to the low crystallinity ones.

3.3. High pressure phase relations

The phase diagrams for the A15R and A17O compositions are shown in Figs. 3 and 4. The results for each capsule material are plotted separately, because the phase relations depend on the type of capsule material used in

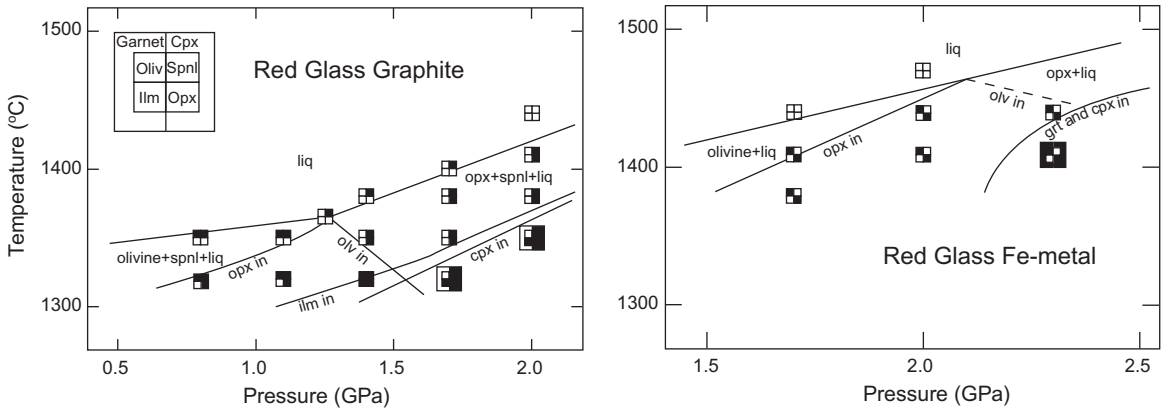

Fig. 3. Phase diagrams of the composition A15R for experiments performed in Fe-metal and graphite capsules. Note the difference in olivine–opx multiple saturation for the different capsule types.

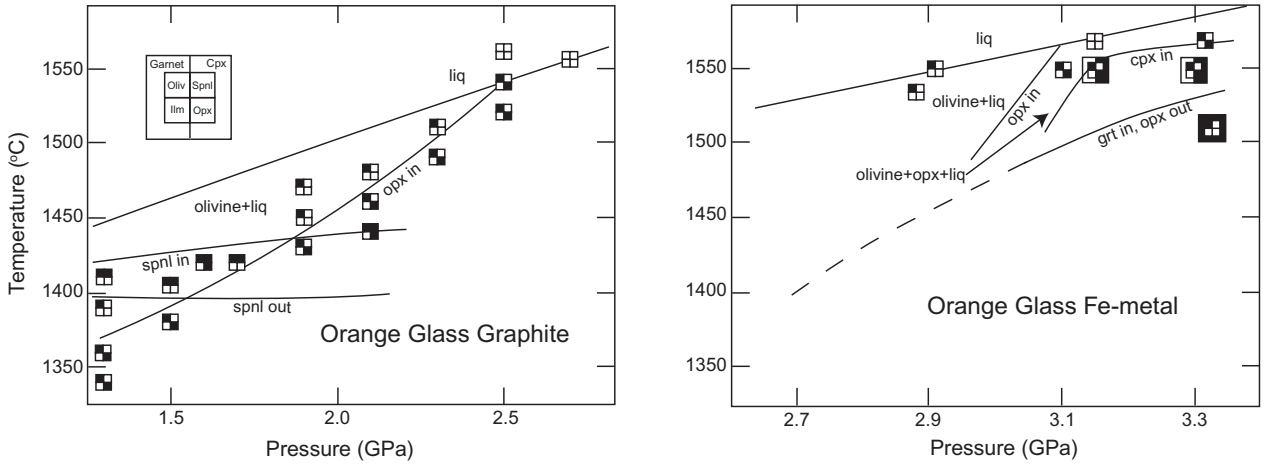

Fig. 4. Phase diagrams of the composition A17O for experiments performed in Fe-metal and graphite capsules. Note that the difference in olivine–opx multiple saturation for the different capsule types is smaller than for the A15R composition.

the piston cylinder experiment. The most striking difference between the graphite and Fe capsule experiments is the change in the extents of the stability fields of olivine and pyroxene on the liquidus.

3.3.1. Apollo 15 red glass

In graphite capsules the A15R composition has a titanium-rich chromium spinel on the liquidus at all pressures, but the modal abundance of this phase is never more than 1–2% of any experiment and usually <1%. Olivine is the next phase to appear at pressures <1.2 GPa, and opx is the next phase to appear after the Ti-rich chromite at pressures >1.3 GPa. The A15R glass is saturated with both olivine and opx at its liquidus at 1.3 GPa and ~1350 °C.

When spec-pure Fe capsules are used the phase relations change significantly. Cr–Ti-rich spinel is no longer the liquidus phase. The maximum pressure of olivine stability in the graphite capsules was an experiment at 1.4 GPa and the highest pressure with olivine as the first silicate to crystallize is 1.3 GPa. In the Fe-capsule, low f_{O_2} experiments, the olivine stability field expands and olivine is stable at pressures at least up to 2.3 GPa. Although there are no experiments with only olivine or opx, experiment C326 at 1.7 GPa has more abundant olivine than opx, and experiment C322 at 2.3 GPa has more abundant opx than olivine. Based on the phase proportions of these near liquidus experiments and assuming a similar topology of our phase relations to those of Delano (1980) we infer at 2.2 GPa and 1450 °C both olivine and opx co-saturate on the liquidus, an increase of 0.9 GPa over the graphite capsules.

Garnet is stable near the liquidus, and is rich in Cr and Ti (Table 4). The Cr–Ti rich garnets that crystallized from the highest-pressure experiments do not remain stable during pressure-quenching. The breakdown of garnet produced a glass with a garnet-like composition and sub-micron sized Cr-rich spinel that likely exsolved from the garnet. These garnet-like areas show Raman spectral characteristics of amorphous material with three broad and weak peaks at 580, 670, and 750 cm^{-1}. The composition of the garnets were reconstituted by using broad beam (10–20 μm) electron microprobe analyses on the amorphous regions overlapping with the small Cr-spinel inclusions. Compositions of garnets from an experiment that was not pressure-quenched, and thus survived the quenching, were similar

Table 4
EMP analyses of A15R experiments in oxide weight percents.

Run	Phase	n[a]	SiO_2[b]		TiO_2		Al_2O_3		Cr_2O_3		FeO		MnO		MgO		CaO		Na_2O		Total
C321	glass	29	35.1	0.23	14.41	0.23	7.43	0.13	0.73	0.04	22.7	0.3	0.25	0.03	10.75	0.22	8.36	0.18	0.35	0.06	100.10
	olv	12	37.7	0.34	0.23	0.01	0.12	0.01	0.40	0.01	22.3	0.4	0.18	0.02	39.05	0.59	0.26	0.01	–	–	100.19
	opx	10	52.3	0.75	1.57	0.22	4.05	0.72	0.81	0.08	13.9	0.3	0.19	0.02	25.99	0.60	1.95	0.07	0.05	0.01	100.78
C322	glass	28	34.8	0.69	14.55	0.46	7.50	0.21	0.73	0.06	22.9	0.6	0.25	0.04	10.96	0.25	8.50	0.22	0.31	0.09	100.49
	olv	4	38.1	0.28	0.24	0.04	0.11	0.01	0.41	0.01	22.2	0.3	0.23	0.04	38.79	0.30	0.27	0.04	0.02	0.02	100.38
	opx	4	52.2	0.06	1.65	0.06	4.24	0.14	0.88	0.02	13.5	0.2	0.16	0.03	26.20	0.29	2.01	0.08	0.06	0.03	100.92
C323	glass	43	32.0	0.33	17.57	0.59	7.42	0.10	0.65	0.05	24.3	0.6	0.27	0.04	9.07	0.15	8.27	0.18	0.46	0.09	100.04
	olv	12	37.6	0.22	0.28	0.04	0.18	0.16	0.33	0.02	24.0	0.4	0.23	0.01	37.30	0.27	0.31	0.06	–	–	100.17
	opx	6	50.9	0.64	1.78	0.21	5.05	0.61	0.86	0.09	15.3	0.4	0.18	0.02	23.84	0.45	2.24	0.11	0.04	0.03	100.18
	cpx	17	50.0	0.46	2.11	0.25	5.10	0.53	0.91	0.06	13.8	0.5	0.21	0.04	19.06	0.55	8.84	0.65	0.29	0.03	100.24
	gnt	15	38.9	0.19	3.02	0.19	20.17	0.25	2.55	0.12	15.3	0.3	0.32	0.02	14.39	0.29	6.26	0.19	0.00	0.01	100.90
C324	glass	11	34.5	0.57	13.82	0.82	7.73	0.27	0.71	0.08	23.4	0.6	0.31	0.02	9.57	0.29	8.85	0.29	0.42	0.08	99.34
	olv	8	38.2	0.36	0.20	0.06	0.12	0.11	0.38	0.04	23.7	1.9	0.21	0.04	37.13	0.98	0.30	0.07	–	–	100.22
	opx	7	50.9	0.83	1.71	0.24	4.38	0.68	1.02	0.10	15.5	0.7	0.20	0.04	25.13	0.29	2.12	0.31	0.02	0.03	100.99
C326	glass	27	35.5	1.99	14.46	0.77	7.79	0.76	0.64	0.40	22.9	1.4	0.26	0.12	9.75	1.37	8.69	0.65	0.34	0.19	100.38
	olv	10	38.1	0.59	0.25	0.06	0.11	0.03	0.38	0.06	23.4	0.7	0.20	0.05	38.14	0.82	0.29	0.05	–	–	100.92
	opx	5	51.4	0.73	1.69	0.26	4.18	0.43	0.88	0.09	14.6	0.4	0.17	0.02	25.67	0.78	2.02	0.36	0.05	0.02	100.62
C329	glass	15	35.6	0.51	13.57	0.64	7.23	0.37	0.72	0.10	22.9	0.7	0.30	0.05	11.25	0.40	8.13	0.25	0.36	0.13	100.11
	olv	5	38.8	0.74	0.23	0.04	0.13	0.04	0.38	0.03	21.3	0.8	0.19	0.03	39.57	0.40	0.27	0.04	–	–	100.87
	opx	5	52.0	0.44	1.55	0.35	3.82	0.94	0.74	0.12	13.7	0.3	0.15	0.03	26.93	0.44	1.93	0.18	0.06	0.04	100.97
C333	glass	20	35.3	0.65	13.06	0.66	7.08	0.22	0.73	0.07	24.0	0.9	0.26	0.14	12.11	0.34	7.79	0.36	0.32	0.10	100.70
C346	glass	15	36.0	0.33	13.53	0.20	7.10	0.08	0.70	0.03	21.7	0.2	0.23	0.02	12.16	0.09	7.77	0.08	0.37	0.05	99.56
B1058	glass	12	39.8	0.28	12.76	0.21	6.39	0.07	3.41	0.21	16.7	0.4	0.27	0.02	10.80	0.12	8.57	0.18	0.37	0.05	99.12
	sp	17	0.1	0.03	7.30	1.24	4.73	1.55	57.41	3.54	21.6	0.4	0.30	0.02	8.97	0.63	0.02	0.01	–	–	100.46
	FeCr	19	–	–	–	–	–	–	3.16	0.60	99.0	0.9	–	–	–	–	–	–	–	–	102.15
C361	glass	19	35.9	0.35	14.05	0.35	7.14	0.07	0.74	0.05	21.9	0.4	0.24	0.02	12.25	0.49	7.90	0.19	0.37	0.07	100.57
	PtFe	16	–	–	–	–	–	Pt:	83.77	0.34	18.3	0.3	–	–	–	–	–	–	–	–	102.03
B1025	glass	20	36.4	0.40	13.90	0.18	7.36	0.12	0.45	0.03	21.6	0.3	0.26	0.02	11.31	0.12	8.13	0.12	0.29	0.14	99.72
	olv	3	38.8	0.13	0.23	0.03	0.04	0.00	0.28	0.01	20.2	0.5	0.21	0.02	41.07	0.24	0.24	0.02	–	–	101.07
	sp																				
B1027	glass	15	37.5	0.31	14.73	0.05	8.25	0.22	0.22	0.06	20.9	0.1	0.27	0.03	8.33	0.47	9.18	0.22	0.40	0.02	99.71
	olv	10	38.2	0.29	0.28	0.06	0.06	0.01	0.21	0.02	22.5	0.6	0.21	0.03	38.20	0.42	0.25	0.02	–	–	99.89
	opx	10	50.9	0.41	1.89	0.41	3.60	0.12	0.86	0.03	15.4	0.3	0.27	0.02	22.48	0.14	4.01	0.18	0.02	0.06	99.48
C309	glass	15	32.3	0.45	17.47	0.39	7.61	0.19	0.41	0.05	22.0	0.6	0.27	0.02	10.06	0.34	9.60	0.33	0.32	0.09	100.03
	opx	10	51.2	0.79	1.13	0.15	4.89	0.81	0.90	0.12	15.0	0.2	0.21	0.02	24.63	0.38	2.32	0.04	0.11	0.05	100.30
	cpx	10	49.6	0.66	1.76	0.15	6.05	0.39	0.96	0.08	12.6	0.6	0.22	0.02	18.35	0.83	10.66	1.15	0.30	0.04	100.48
	ilm	7	0.1	0.02	51.51	0.35	1.99	0.04	4.84	0.09	32.4	0.5	0.22	0.03	7.93	0.07	0.29	0.03	–	–	99.32
	sp	8	0.2	0.01	11.52	0.18	21.91	0.55	22.92	0.57	32.3	0.2	0.21	0.03	10.46	0.13	0.12	0.05	–	–	99.75
C310	glass	15	32.6	0.31	15.88	0.55	8.34	0.15	0.27	0.03	24.1	0.7	0.28	0.03	8.99	0.64	9.26	0.55	0.47	0.14	100.30
	opx	10	49.3	0.32	1.41	0.08	6.26	0.47	0.81	0.03	16.7	0.3	0.23	0.02	23.17	0.32	2.34	0.11	0.03	0.03	100.25
	cpx	15	48.6	0.52	1.91	0.19	6.57	0.53	0.76	0.05	13.8	0.5	0.22	0.02	17.31	0.72	10.41	0.92	0.18	0.03	99.76
	ilm	6	0.2	0.08	53.17	0.32	1.60	0.08	2.85	0.13	34.3	0.2	0.24	0.02	7.38	0.31	0.29	0.05	–	–	100.05
	sp	7	0.3	0.01	10.85	0.26	26.64	0.49	19.36	0.16	32.5	0.2	0.21	0.02	10.22	0.14	0.11	0.03	–	–	100.13

C311	glass	15	34.5	0.31	16.32	0.40	7.51	0.18	0.68	0.05	19.2	0.3	0.29	0.03	12.07	0.54	8.69	0.40	0.33	0.11	99.57
	opx	10	52.1	0.55	1.03	0.07	4.34	0.37	1.21	0.08	13.0	0.3	0.21	0.02	26.40	0.47	1.84	0.13	0.09	0.04	100.22
	sp	4	0.3	0.02	7.54	0.43	20.01	0.23	34.33	0.66	26.4	0.2	0.19	0.02	10.78	0.59	0.06	0.02	–	–	99.66
C312	glass	15	34.2	0.67	16.15	0.71	7.42	0.13	0.53	0.04	20.0	0.5	0.28	0.02	12.25	0.35	8.37	0.31	0.16	0.11	99.41
	opx	11	51.2	0.45	1.23	0.07	4.25	0.18	1.02	0.06	13.4	0.2	0.18	0.02	26.27	0.55	1.97	0.19	0.05	0.02	99.58
	sp	4	0.2	0.02	10.33	0.12	18.07	0.97	30.47	0.64	28.8	0.1	0.25	0.03	10.82	0.71	0.07	0.01	–	–	99.07
C313	glass	15	36.8	0.28	14.73	0.26	7.41	0.18	0.85	0.07	19.1	0.7	0.23	0.04	13.84	0.92	7.77	0.50	0.24	0.05	100.87
	opx	1	52.4		1.02		4.12		1.32		12.8		0.18		27.87		1.66		0.03		101.41
	sp	1	0.3		7.29		13.49		38.33		24.8		0.25		13.07		0.16		0.07		97.69
C314	glass	3	36.6	0.19	14.80	0.19	7.55	0.06	0.55	0.04	18.9	0.3	0.23	0.04	11.33	0.06	8.41	0.05	0.51	0.03	98.80
	opx	12	52.6	0.80	1.12	0.12	3.66	0.56	1.11	0.10	12.6	0.3	0.20	0.02	27.38	1.04	1.66	0.17	0.04	0.02	100.30
	sp	6	0.2	0.02	9.29	0.29	15.66	0.86	35.44	0.45	26.9	0.2	0.23	0.03	11.75	0.61	0.11	0.03	–	–	99.50
C315	glass	15	36.3	0.27	13.92	0.31	7.15	0.09	0.79	0.08	20.3	0.6	0.24	0.03	13.26	0.70	7.67	0.34	0.23	0.06	99.90
C316	glass	5	36.3	0.12	13.68	0.16	7.17	0.03	0.58	0.04	20.3	0.4	0.24	0.02	12.24	0.11	7.86	0.09	0.38	0.07	98.70
	sp	6	0.2	0.02	8.59	0.14	15.80	0.21	37.88	0.43	25.5	0.2	0.25	0.02	11.88	0.38	0.17	0.01	–	–	100.20
C317	glass	8	35.6	0.36	14.69	0.24	7.48	0.04	0.41	0.02	20.3	0.1	0.25	0.04	11.06	0.05	8.49	0.04	0.40	0.12	98.70
	opx	16	52.2	0.37	1.19	0.08	3.31	0.15	1.06	0.04	12.7	0.2	0.20	0.03	27.60	0.58	1.57	0.11	0.02	0.02	99.80
	sp	5	0.2	0.02	10.72	0.07	14.79	0.16	33.26	0.21	28.1	0.4	0.20	0.04	11.74	0.33	0.12	0.05	–	–	99.10
C318	glass	3	36.2	0.12	15.10	0.57	8.11	0.22	0.28	0.08	19.6	0.2	0.28	0.02	10.42	0.46	8.79	0.27	0.42	0.05	99.27
	olv	4	38.6	0.33	0.26	0.07	0.07	0.01	0.21	0.02	20.1	0.4	0.24	0.04	40.50	0.27	0.25	0.01	–	–	100.26
	opx	5	52.7	0.20	1.43	0.08	3.50	0.16	1.03	0.04	13.1	0.3	0.20	0.03	27.16	0.40	1.59	0.11	0.04	0.02	100.73
	sp	4	0.2	0.01	12.55	0.31	12.52	0.20	31.09	0.22	30.1	0.2	0.26	0.01	11.72	0.12	0.13	0.05	–	–	98.63
C320	glass	18	37.0	0.27	13.42	0.30	7.06	0.08	0.49	0.04	20.9	0.2	0.25	0.03	11.48	0.15	7.73	0.15	0.54	0.09	98.86
	olv	12	38.9	0.27	0.19	0.04	0.09	0.02	0.30	0.05	19.8	0.4	0.19	0.03	39.94	0.28	0.22	0.01	–	–	99.63
	sp	7	0.1	0.02	11.78	0.20	12.47	0.14	36.35	0.45	27.7	0.3	0.23	0.02	10.78	0.47	0.10	0.03	–	–	99.52
C332	glass	46	33.7	0.44	15.95	0.22	7.88	0.08	0.25	0.03	22.2	0.2	0.27	0.03	8.79	0.12	9.49	0.15	0.45	0.08	98.94
	olv	12	38.1	0.40	0.36	0.41	0.11	0.05	0.17	0.03	23.8	0.4	0.24	0.03	36.93	0.37	0.28	0.02	–	–	99.99
	opx	12	51.4	0.61	1.33	0.12	4.22	0.47	0.85	0.10	14.7	0.2	0.20	0.02	25.63	0.60	2.19	0.09	0.06	0.02	100.65
	ilm	10	0.1	0.02	53.96	0.41	1.30	0.03	3.44	0.12	31.7	0.5	0.23	0.02	9.26	0.30	0.12	0.03	–	–	100.12
	sp	4	0.2	0.03	15.44	0.10	15.88	0.39	22.60	0.12	35.0	0.1	0.23	0.02	10.33	0.33	0.14	0.05	–	–	99.76

[a] n = number of probe analyses.

[b] Columns directly following the oxide wt% are 1-σ errors from replicate analyses.

Table 5
EMP analyses of A17O experiments in oxide weight percents.

Run	Phase	*n*	SiO_2		TiO_2		Al_2O_3		Cr_2O_3		FeO		MnO		MgO		CaO		Na_2O		Total
D176	glass	15	39.3	0.18	10.39	0.17	6.48	0.05	0.61	0.05	20.2	0.3	0.28	0.03	14.15	0.20	8.38	0.13	0.32	0.10	100.11
	olv	10	39.2	0.14	0.17	0.02	0.10	0.01	0.30	0.02	17.3	0.3	0.19	0.02	42.97	0.30	0.27	0.02	–	–	100.46
	opx	10	54.1	0.31	0.89	0.08	2.75	0.27	0.51	0.03	12.1	0.2	0.19	0.03	28.28	0.30	2.08	0.03	0.09	0.05	101.01
D187	glass	15	32.1	0.25	16.75	0.28	5.47	0.07	0.53	0.04	26.9	0.4	0.30	0.02	10.02	0.14	7.65	0.16	0.33	0.07	100.08
	olv	9	37.5	0.30	0.25	0.03	0.17	0.15	0.27	0.02	24.4	0.6	0.24	0.03	36.62	0.35	0.34	0.04	–	–	99.89
	cpx	15	51.5	0.30	1.38	0.07	3.52	0.18	0.53	0.03	14.0	0.4	0.24	0.02	20.09	0.51	8.75	0.76	0.22	0.05	100.20
	gnt	11	38.8	1.15	3.52	0.58	19.28	0.69	1.78	0.59	15.9	0.6	0.35	0.02	12.43	0.98	7.21	0.58	0.09	0.04	99.37
D190	glass	15	36.7	0.19	11.52	0.17	6.75	0.09	0.66	0.03	23.4	0.3	0.26	0.04	12.04	0.16	8.41	0.12	0.38	0.08	100.23
	olv	10	38.4	0.19	0.17	0.02	0.13	0.01	0.32	0.01	20.9	0.3	0.26	0.02	39.53	0.17	0.32	0.01	–	–	100.00
	opx	7	53.1	0.51	0.89	0.11	3.16	0.39	0.60	0.05	13.9	0.3	0.21	0.01	26.53	0.26	2.39	0.10	0.11	0.03	100.90
	cpx	14	52.5	0.20	1.05	0.07	3.46	0.17	0.63	0.02	13.4	0.4	0.25	0.03	23.21	0.49	6.20	0.42	0.20	0.04	100.89
C408	glass	14	36.1	0.18	8.36	0.12	5.42	0.09	0.56	0.02	29.1	0.2	0.25	0.02	13.57	0.17	6.96	0.14	0.27	0.11	100.69
	olv	5	37.9	0.43	0.12	0.03	0.11	0.02	0.28	0.03	23.2	0.6	0.21	0.02	38.28	0.51	0.32	0.02	–	–	100.45
D195	glass	15	39.3	0.17	8.85	0.15	5.84	0.05	0.61	0.03	21.7	0.2	0.31	0.02	15.47	0.16	7.28	0.14	0.22	0.09	99.55
D198	glass	28	37.4	0.33	10.74	0.33	6.64	0.12	0.64	0.05	23.0	0.40	0.30	0.02	12.66	0.19	8.65	0.15	0.25	0.07	100.24
	olv	12	38.0	0.26	0.23	0.02	0.13	0.01	0.34	0.02	20.8	0.2	0.21	0.03	40.61	0.32	0.33	0.01	–	–	100.63
	opx	12	53.4	0.48	0.71	0.14	2.97	0.48	0.35	0.04	13.5	0.4	0.14	0.02	26.74	0.36	2.31	0.15	0.07	0.03	100.13
	cpx	15	53.0	0.47	0.98	0.08	3.14	0.21	0.54	0.02	13.0	0.7	0.21	0.03	24.24	0.73	5.57	0.94	0.13	0.03	100.86
D199	glass	13	39.0	0.16	9.57	0.19	6.11	0.10	0.67	0.03	22.6	0.3	0.29	0.03	14.34	0.17	8.14	0.05	0.19	0.03	100.89
	olv	8	38.9	0.45	0.21	0.02	0.15	0.03	0.33	0.03	19.2	0.4	0.19	0.02	41.47	0.38	0.29	0.02	–	–	100.77
	opx	12	54.4	0.47	0.70	0.11	2.65	0.43	0.29	0.03	12.0	0.2	0.14	0.02	28.37	0.42	1.99	0.05	0.06	0.02	100.61
B1050	glass	5	38.8	0.31	9.65	0.40	6.29	0.23	0.66	0.08	22.7	0.5	0.25	0.03	12.43	0.25	7.86	0.26	0.27	0.14	98.86
	olv	5	38.4	0.28	0.11	0.06	0.07	0.01	0.29	0.03	20.5	0.7	0.23	0.04	40.60	0.58	0.24	0.04	–	–	100.44
C363	glass	27	37.1	0.38	11.27	0.23	7.11	0.10	0.42	0.04	23.8	0.3	0.28	0.03	9.89	0.31	9.25	0.12	0.42	0.07	99.54
	olv	12	37.3	0.29	0.20	0.05	0.08	0.01	0.20	0.02	24.5	0.2	0.27	0.03	36.69	0.41	0.34	0.02	–	–	99.57
	opx	14	52.8	0.76	0.99	0.12	2.88	0.69	1.01	0.18	14.8	0.2	0.22	0.02	25.70	0.41	2.20	0.13	0.01	0.02	100.59
	sp	4	0.2	0.02	10.55	0.12	14.70	0.31	31.46	0.39	31.1	0.5	0.27	0.04	9.55	0.33	0.10	0.04	–	–	97.92
C364	glass	14	37.8	0.44	11.20	0.68	7.39	0.17	0.34	0.07	23.1	0.5	0.26	0.06	10.02	0.29	9.00	0.22	0.39	0.08	99.47
	olv	13	37.6	0.56	0.13	0.04	0.08	0.03	0.23	0.05	24.0	0.7	0.22	0.03	37.01	0.83	0.27	0.03	–	–	99.62
	opx	10	52.8	0.57	0.90	0.08	2.67	0.46	0.92	0.13	14.5	0.3	0.19	0.02	25.82	0.47	1.92	0.11	0.01	0.01	99.75
	sp	2	0.5	0.36	9.85	0.05	12.74	0.28	34.2	0.11	31.9	0.1	0.34	0.02	9.79	0.62	0.12	0.02	–	–	99.51
C365	glass	11	37.7	0.44	11.20	0.44	7.29	0.16	0.32	0.04	23.0	0.3	0.25	0.02	9.81	0.55	9.04	0.21	0.39	0.05	99.08
	olv	11	37.9	0.32	0.21	0.05	0.09	0.01	0.22	0.04	24.5	0.4	0.21	0.02	35.73	0.49	0.32	0.02	–	–	99.19
	opx	12	52.3	0.46	1.03	0.06	3.08	0.32	0.98	0.09	14.7	0.2	0.17	0.02	25.34	0.30	2.01	0.14	0.01	0.01	99.58
	sp	3	0.3	0.16	11.09	0.18	13.02	0.13	31.3	0.16	33.0	0.2	0.27	0.02	9.51	0.06	0.21	0.03	–	–	98.77
C366	glass	13	38.9	0.22	9.68	0.21	6.73	0.07	0.60	0.05	22.5	0.2	0.24	0.03	11.91	0.12	7.93	0.12	0.58	0.07	99.05
	olv	11	38.1	0.26	0.15	0.02	0.09	0.01	0.35	0.02	21.8	0.1	0.18	0.03	38.37	0.25	0.26	0.01	0.01	0.01	99.33
	sp																				
C367	glass	18	40.3	0.85	9.47	0.53	6.85	0.13	0.66	0.15	21.4	1.2	0.26	0.03	13.42	0.59	8.11	0.33	0.29	0.09	100.79
	olv	11	38.1	0.27	0.10	0.03	0.08	0.01	0.30	0.02	21.5	0.3	0.17	0.03	38.66	0.24	0.24	0.01	–	–	99.13
	sp	8	0.2	0.06	7.63	0.35	11.95	0.61	40.51	0.77	27.3	0.9	0.29	0.06	10.64	0.77	0.08	0.04	–	–	98.85
C368	glass	13	39.0	0.24	9.65	0.19	6.70	0.05	0.56	0.05	22.5	0.3	0.25	0.03	12.12	0.23	7.88	0.17	0.36	0.05	99.05
	olv	10	38.4	0.34	0.10	0.01	0.07	0.01	0.30	0.01	21.1	0.2	0.18	0.02	38.93	0.49	0.23	0.01	–	–	99.32

	sp	7	0.2	0.01	7.79	0.05	11.86	0.30	41.44	0.24	27.2	0.3	0.27	0.02	9.85	0.17	0.11	0.02	–	–	99.06
C370	glass	2	38.7	0.39	9.70	0.05	6.43	0.04	0.72	0.10	22.4	0.3	0.25	0.03	12.11	0.08	8.02	0.12	0.34	0.03	98.65
	olv	4	38.5	0.53	0.11	0.02	0.07	0.01	0.28	0.01	21.5	0.6	0.19	0.03	39.36	0.21	0.24	0.02	–	–	100.29
	opx	4	53.4	0.43	0.79	0.03	2.65	0.25	1.16	0.04	13.4	0.3	0.15	0.02	27.49	0.29	1.69	0.14	0.00	0.01	100.73
	sp	4	0.2	0.03	7.63	0.14	12.63	0.42	39.95	0.69	27.8	0.4	0.24	0.02	10.65	0.24	0.04	0.03	–	–	99.19
C371	glass	16	38.0	0.29	10.01	0.20	6.70	0.07	0.70	0.05	23.3	0.2	0.28	0.03	11.95	0.21	8.42	0.13	0.45	0.11	99.80
	olv	15	38.0	0.33	0.11	0.03	0.08	0.01	0.32	0.02	22.1	0.3	0.21	0.02	39.26	0.36	0.26	0.01	–	–	100.30
	opx	14	53.4	0.58	0.76	0.10	2.64	0.41	1.13	0.14	13.4	0.2	0.20	0.03	27.23	0.56	1.83	0.05	0.06	0.03	100.60
C373	glass	19	36.2	0.36	11.07	0.19	6.88	0.10	0.63	0.05	24.8	0.5	0.30	0.04	10.28	0.61	9.12	0.17	0.40	0.10	99.67
	olv	13	37.4	0.20	0.16	0.03	0.10	0.02	0.28	0.02	23.8	0.3	0.22	0.02	38.57	0.38	0.34	0.02	–	–	100.80
	opx	12	52.6	0.35	0.89	0.03	3.52	0.11	1.18	0.05	14.2	0.2	0.21	0.02	26.25	0.20	2.19	0.15	0.05	0.02	101.10
	sp	7	0.3	0.02	8.64	0.11	17.51	0.61	33.29	0.37	28.4	0.5	0.20	0.05	10.77	0.35	0.13	0.05	–	–	99.24
C376	glass	10	36.9	0.33	9.91	0.25	6.59	0.07	0.63	0.04	23.9	0.5	0.28	0.03	12.10	0.18	8.42	0.10	0.56	0.06	99.32
	olv	16	37.9	0.14	0.12	0.02	0.10	0.01	0.31	0.01	22.2	0.5	0.23	0.03	38.97	0.45	0.28	0.01	–	–	100.08
	opx	14	53.2	0.43	0.71	0.04	2.80	0.23	1.03	0.06	13.4	0.3	0.20	0.02	27.28	0.27	1.84	0.04	0.03	0.02	100.49
C380	glass	43	39.3	0.59	9.47	0.24	6.23	0.10	0.74	0.11	22.1	0.88	0.27	0.03	14.54	0.65	7.80	0.25	0.18	0.06	100.61
	olv	10	38.9	0.25	0.09	0.02	0.10	0.02	0.31	0.01	20.1	0.2	0.20	0.04	39.88	0.20	0.24	0.01	–	–	99.87
C381	glass	16	39.0	0.44	9.67	0.22	6.33	0.10	0.71	0.07	22.0	0.66	0.29	0.02	13.91	0.37	8.18	0.26	0.24	0.07	100.28
	olv	10	38.3	0.17	0.10	0.03	0.09	0.01	0.34	0.02	20.3	0.2	0.20	0.02	39.81	0.25	0.26	0.02	–	–	99.45
C382	glass	11	38.7	0.25	9.68	0.24	6.48	0.04	0.64	0.05	22.3	0.3	0.30	0.03	12.47	0.44	8.05	0.11	0.50	0.15	99.16
	olv	10	38.2	0.30	0.11	0.02	0.09	0.01	0.35	0.01	21.3	0.2	0.20	0.03	39.39	0.37	0.25	0.01	–	–	99.94
C388	glass	16	38.4	0.22	9.63	0.19	6.18	0.10	0.68	0.03	22.9	0.3	0.31	0.03	13.20	0.18	7.93	0.16	0.42	0.07	99.75
	olv	4	39.2	0.16	0.13	0.02	0.07	0.01	0.34	0.01	19.8	0.5	0.22	0.02	40.76	0.23	0.27	0.01	–	–	100.87
	opx	5	54.3	0.60	0.61	0.12	2.27	0.52	0.85	0.14	12.3	0.1	0.17	0.02	28.15	0.37	1.75	0.03	0.14	0.05	100.55
C389	glass	13	39.0	0.50	8.97	0.14	6.18	0.07	0.71	0.05	22.1	0.5	0.27	0.03	13.69	0.36	8.12	0.15	0.40	0.14	99.38
	olv	14	38.3	0.23	0.10	0.03	0.09	0.01	0.31	0.01	19.8	0.3	0.18	0.03	41.17	0.28	0.26	0.02	–	–	100.18
C395	glass	12	38.7	0.60	9.47	0.25	6.21	0.13	0.73	0.08	22.5	0.9	0.28	0.04	14.80	0.45	8.14	0.33	0.13	0.08	100.99
	olv	15	38.4	0.28	0.10	0.03	0.09	0.01	0.29	0.02	19.9	0.3	0.18	0.02	41.18	0.42	0.26	0.01	–	–	100.32
	opx	11	53.8	0.40	0.61	0.07	2.52	0.29	0.87	0.09	12.3	0.3	0.16	0.04	28.51	0.47	1.74	0.04	0.03	0.02	100.55
C396	glass	19	39.9	1.10	8.79	0.61	6.51	0.16	0.81	0.09	21.2	1.3	0.29	0.03	15.19	0.80	7.77	0.26	0.29	0.09	100.83
	olv	12	38.3	0.50	0.11	0.02	0.11	0.02	0.30	0.01	20.1	0.2	0.21	0.02	40.56	0.59	0.26	0.01	–	–	99.96
	opx	10	54.4	0.49	0.63	0.06	2.73	0.26	0.88	0.08	12.3	0.2	0.18	0.03	28.10	0.38	1.67	0.16	0.03	0.01	100.92
C397	glass	16	38.5	0.18	8.55	0.17	5.71	0.05	0.68	0.04	23.1	0.2	0.25	0.03	15.41	0.16	7.40	0.13	0.23	0.07	99.86
C409	glass	17	38.8	0.80	8.95	0.32	5.89	0.14	0.72	0.08	22.0	1.0	0.25	0.02	16.12	1.11	7.43	0.37	0.34	0.43	100.65

to the broad beam analyses of exsolved and decomposed garnets.

3.3.2. Apollo 17 orange glass

In Fig. 4 the influence of capsule material on phase equilibria is shown for the A17O starting material. In graphite capsules, the A17O composition is saturated on its liquidus with olivine and opx at 2.5 GPa and ~1530 °C. At lower pressure, olivine is the liquidus phase and at higher pressure we infer opx as the liquidus phase. For Fe capsules the olivine stability field expands and olivine is the liquidus phase at pressures up to 3.1 GPa. At 3.1 GPa and ~1560 °C olivine and opx are stable at the liquidus. Olivine coexisting with opx is the stable liquidus assemblage to at least 3.3 GPa. Clinopyroxene (sub-calcic augite) and garnet are also stable near the liquidus at pressures >3.1 GPa. The difference in MSPs between graphite and Fe capsules for the A17O glass is 0.6 GPa, smaller than the 0.9 GPa of the A15R glass.

3.4. Comparison to previous experimental studies

The phase relations of the A15R glass were determined by Delano (1980), and those of the A17O glass were determined by Green et al. (1975). In both of these experimental studies experimental durations were short (5–120 min) compared to the experimental durations used in this study. In addition, the experiments of Green et al. (1975) were run in a 'mild steel' capsule, an Fe–C alloy that will produce a smelting reaction, reducing FeO in the melt to Fe-metal, significantly changing the bulk composition of the silicate portion of the starting material. Our experiments were carried out in graphite and spec-pure Fe capsules. These capsule materials remain relatively inert with respect to the bulk composition of the silicate portion of the sample and also control the f_{O_2} of our system (see Section 3.1).

Experiments on the A15R glass in spec-pure Fe capsules are generally similar to those by Delano (1980), who also used spec-pure Fe capsules. Our experiments produce an olivine–opx multiple saturation point at 2.2 GPa. At similar P and T conditions our boundaries for olivine and opx stability are slightly different than those of Delano (1980), however the inferred point of coexistence of opx and olivine on the liquidus in our experiments is within 0.2 GPa of Delano (~2.4 GPa). The main difference between our Fe capsule results and those of Delano is the presence of garnet near the liquidus.

The results on the A15R glass in graphite differ from those of Delano (1980) in several respects. The liquidus phase is an oxide and not olivine or opx. Another difference is that the MSP of olivine–opx is much lower in pressure (1.3 GPa). Ilmenite joins the crystallization sequence at lower temperatures, well below the liquidus, and after a Cr–Ti spinel saturates, which is consistent with what Delano (1980) observed. A high calcium clinopyroxene joins the crystallizing assemblage of opx + spnl + ilmenite and the liquids in equilibrium with this assemblage may be analogous to low degree melts of late stage magma ocean cumulates.

The MSP of the Apollo 17 orange glass occurs at the highest pressure of the three high-Ti glasses that have been experimentally studied, and ranges from 2.5 GPa in graphite capsules to 3.1 GPa for the Fe metal capsules. Like the A15R glass, there is garnet near the liquidus at high pressure in the Fe capsule runs. In the highest pressure and temperature experiments attempted here a sub-calcic augite is a near-liquidus pyroxene phase. The lower calcium content of the clinopyroxene is a function of the higher liquidus temperatures at these high pressures (Lindsley and Dixon, 1976). Sub-calcic augite is also seen in some experiments on other low-Ti lunar glasses (Elkins-Tanton et al., 2003).

The phase relations reported here are quite different from those reported by Green et al. (1975), who determined a MSP of 2.0 GPa. The MSP of 2.0 GPa is lower than our result at high f_{O_2}, and possibly represents the slow nucleation of olivine and/or possible Fe-loss through reduction of Fe^{2+} by a smelting reaction facilitated by the carbon in the mild steel capsules used by Green et al. (1975). Reduction of the FeO component of the melt leads to SiO_2 enrichment, and stabilizes opx to lower pressures by decreasing the overall $\frac{MgO+FeO}{SiO_2}$ of the melt. However, Green et al. (1975) do not report compositions of minerals or melts, so it is not possible to definitively determine the reasons for the difference observed here.

4. DISCUSSION

4.1. Effects of variable f_{O_2} on phase equilibria

The phase relations of these high-Ti lunar compositions are extremely sensitive to changes in the oxidation state imposed by the graphite and Fe metal capsule materials (Figs. 3 and 4). The reason for the sensitivity is the high abundance of multiple valence elements Ti, Fe, and Cr. We have measured the f_{O_2} of our experiments in order to quantitatively constrain the effect of f_{O_2} variations on the phase equilibria, and ultimately, the inferred depth of origin of such high-Ti magmas.

Both the A17O and A15R starting materials have similar FeO and Cr_2O_3 contents, but have different TiO_2 contents. The controlled amounts of FeO and Cr_2O_3 allows us to examine the effect of variable TiO_2 concentration, oxidation state, and speciation on the pressure of olivine–opx MSPs. The more oxidized experiments show lower pressure MSPs, in both the A17O and A15R glasses. The difference in the MSP for the A15R glass is 50% greater than that observed for the A17O glass over the same range in f_{O_2}, suggesting that the higher TiO_2 content (~40% greater) of the A15R enhances the effects of f_{O_2} on the MSP. Thus we suggest that the black glass of Apollo 14, which has more TiO_2 than the A15R glass (16.4 wt% TiO_2), would show an even greater difference in MSP between graphite and Fe metal capsules (Fig. 5).

We suggest that the f_{O_2} control on olivine–opx equilbria is caused by a shift in the TiO_2:Ti_2O_3 ratio of the experiment because Ti is the only major element that would change valence state at these reducing conditions, as almost all of the Fe is divalent over this range (Kress and Carmichael, 1991). The partition coefficients for TiO_2^* (* indicates all of the element is calculated as a single valence) as measured by electron microprobe are $D_{Ti}^{olv-melt} = 0.017 \pm 0.002$ for A15R and $D_{Ti}^{olv-melt} = 0.014 \pm 0.004$ for A17O. Previous

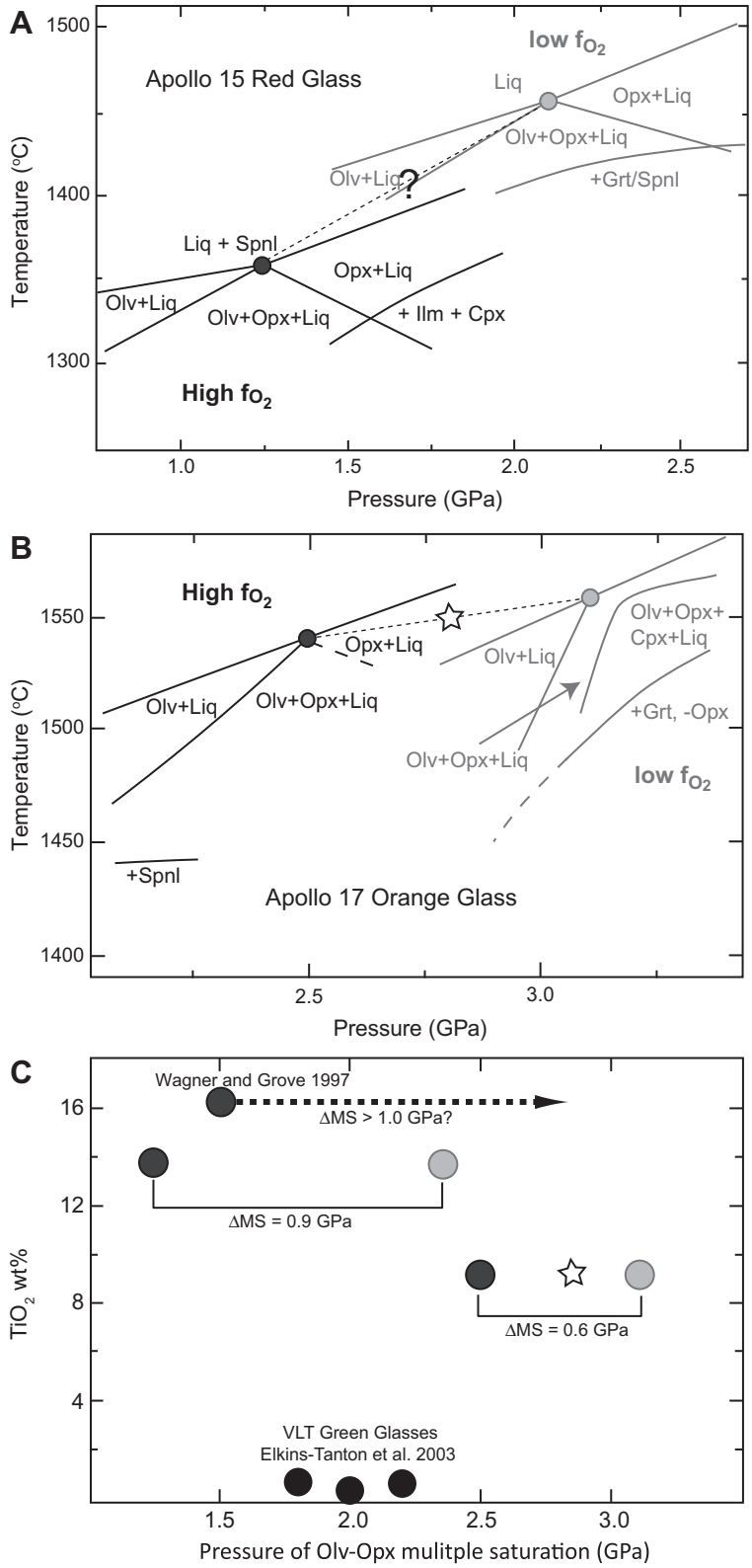

Fig. 5. (A) A simplified diagram showing the phase relations in the A15R for both the graphite (high f_{O_2}) and Fe capsule experiments (low f_{O_2}). The filled circles represent the olivine–opx MSPs, and the question mark is because there are no independent estimates of pre-eruptive f_{O_2} for the A15R. (B) Same as (A) but for the orange glass, the star is the best estimate for source region P and T based on interpolating the experimental MSP's to a f_{O_2} of IW−0.6. (C) Summary of the MSP data for lunar ultramafic glasses. Open symbols are for experiments in Fe capsules and filled are for graphite.

measurements of Ti partition coefficients between melt and olivine on low-Ti starting materials are similar (Colson et al., 1988). The similarity suggests that Ti incorporation in silicates is not a function of TiO_2^* content in the melt. The similarity in the silicate compositions and Ti partitioning at multiple f_{O_2}'s leads us to infer that Ti^{3+} and Ti^{4+} are somehow influencing the melt structure and thus *indirectly* the liquidus silicate phase stability.

Silicate melt structure is known to affect transition metal partitioning between olivine and melt (Kushiro and Mysen, 2002; Mysen, 2007) and f_{O_2} has an effect on the transition metal partitioning as well (Mysen, 2006). These studies have noted that major melt structural parameters—e.g. the non-bridging oxygen-tetrahedrally coordinated cation ratio—correlate with the partitioning behavior. These previous studies have focused on ambient pressure crystallization at oxygen fugacity high enough to significantly change the Fe^{2+}/Fe^{3+}, and on melts that have a wide variety of compositions. Our experiments were conducted at much lower f_{O_2}, and on bulk compositions that do not vary greatly in their ratio of non-bridging oxygens to tetrahedrally coordinated cations, thus variations in the transition metal partitioning between olivine and melt are reflecting the influence of pressure, temperature, and Ti content and oxidation state on the stability of olivine.

4.1.1. Variations in mineral–melt Fe–Mg exchange

The K_D^{Fe-Mg} in most systems for olivine is extremely homogeneous at about 0.3–0.33 (Roeder and Emslie, 1970; Longhi et al., 1978; Toplis, 2005). In experiments on lunar low-Ti ultramafic glasses (Fig. 6) K_D^{Fe-Mg} values are higher, but constant at 0.34–0.35, similar to high iron basalts from Mars (Filiberto and Dasgupta, 2011). In our high-Ti experiments K_D^{Fe-Mg} values range from 0.23 to 0.34. The experimental range in K_D^{Fe-Mg} is consistent with other studies of high-Ti compositions (Longhi et al., 1978; Delano, 1980; Jones, 1988; Wagner and Grove, 1997; Xirouchakis et al., 2001; Canil and Bellis, 2008). The K_D^{Fe-Mg} values are a function of TiO_2 content, pressure and/or temperature, as well as f_{O_2}. It is not possible to separate the effects of pressure and temperature in our experiments because the high pressure experiments with olivine and liquid are also the high temperature experiments. The pressure/temperature effect was first observed by Delano (1980) who found that with increasing pressure the K_D^{Fe-Mg} becomes more 'normal' approaching the 0.34 value.

The K_D^{Fe-Mg}'s show a variation with f_{O_2} and show a negative correlation with bulk Ti content. There are several others who have noted the negative correlation of olivine K_D^{Fe-Mg} with increasing TiO_2^* in the melt (Longhi et al., 1978; Delano, 1980; Jones, 1988; Xirouchakis et al., 2001). However other authors have suggested that it is not the increased Ti content that affects the K_D^{Fe-Mg}, but actually the low silica contents that necessarily accompany the increased Ti (Longhi et al., 1978; Toplis, 2005). Our new results show the K_D^{Fe-Mg} is strongly influenced by lowering the f_{O_2} (Fig. 6), as olivines in Fe-capsule runs show distinctly lower K_D^{Fe-Mg} than graphite capsule runs at the same pressure and temperature. The dependence of K_D^{Fe-Mg} values on f_{O_2} indicates Ti^{3+} in the melt is a component that is influencing the K_D^{Fe-Mg} in these high-Ti–low-silica liquids, because Si will be only tetravalent under both f_{O_2}

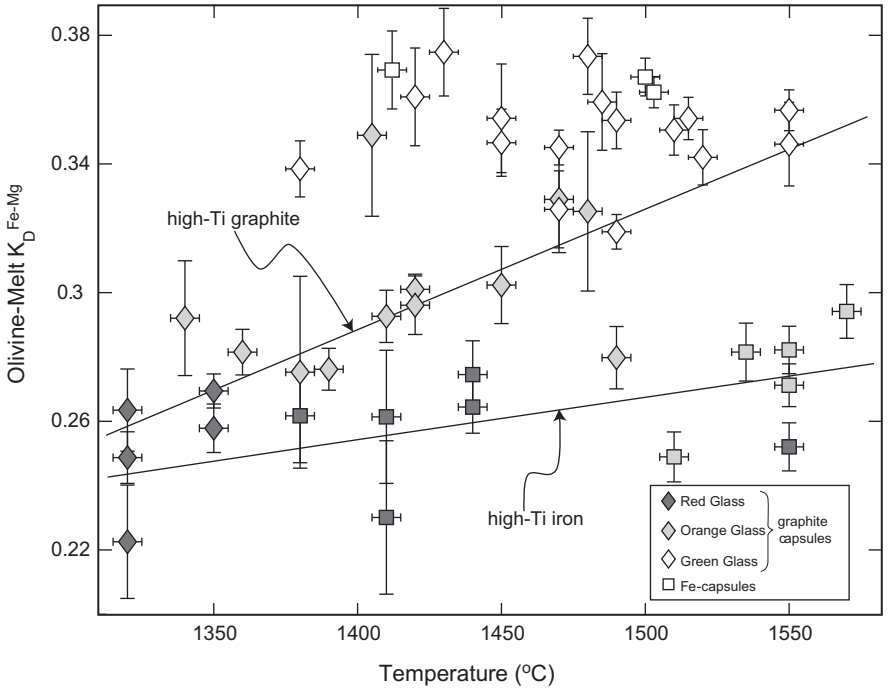

Fig. 6. The olivine–melt Fe–Mg exchange coefficient for each experiment is plotted versus the experimental temperature. Green glasses from Elkins-Tanton et al. (2003) and Red and Orange glasses are from Tables 4 and 5. Diamonds are graphite capsule experiments and squares are Fe-metal experiments. The lines shown are the best fit linear regressions to the high-Ti graphite and high-Ti Fe capsule experiments.

conditions. Thus we can rule out silica activity as the sole control on the low K_D^{Fe-Mg} (Toplis, 2005).

The equation for K_D^{Fe-Mg} can be written as the product of ratios of MgO and FeO in the melt and olivine (X):

$$K_D^{Fe-Mg} = \frac{X_{Fe}^{olv}}{X_{Mg}^{olv}} \cdot \frac{X_{Mg}^{melt}}{X_{Fe}^{melt}} \quad (3)$$

The change in the K_D^{Fe-Mg} exchange coefficient value provides insight into the silicate melt speciation. A low value of K_D^{Fe-Mg} (i.e. 0.23) signifies that the olivine is more forsteritic than expected for a crystal in equilibrium with a melt of a particular Fe/Mg ratio. The ratio of $X_{Fe}^{olv}/X_{Mg}^{olv}$ (i.e. the olivine composition) in our experiments does not vary enough to account for the shift of the K_D^{Fe-Mg} from 0.34 to 0.23. In order to raise the K_D^{Fe-Mg} from experimental values to the expected value of 0.34, either less of the FeO in the melt must be available to create olivine (i.e. X_{Fe}^{melt} goes down) or more MgO in the melt is available to the olivine (i.e. X_{Mg}^{melt} goes up).

Complexing Ti with Fe is one way to lower the amount of olivine-compatible FeO in the melt because Ti is an incompatible element in olivine. Jones (1988) first tried to explore the implications of Fe–Ti coupling in lowering the K_D^{Fe-Mg}, and suggested that a melt component similar to ferropseudobrookite ($FeTi_2O_5$) was present. Our experiments show that at lower f_{O_2} the K_D^{Fe-Mg} is further depressed, suggesting that small amounts of Ti^{3+} in the melt might significantly stabilize a Fe–Ti melt component to higher temperatures. Similar behavior of Ti^{3+} has been observed in stabilizing the solid solutions of Fe–Ti oxides like armalcolite (Kesson and Lindsley, 1975).

4.1.2. The Ti^{3+} effect on MSP's

We have adapted the projection scheme from Longhi et al. (1974) for displaying the bulk rock compositions of high-Ti basalts as a projection through an Fe–Ti oxide phase onto the plag + cpx–quartz–olivine plane (Fig. 7). The projection allows us to examine the position of Ti-absent silicate phase boundaries for bulk compositions of widely varying Ti content. By projecting through an Fe,Mg–Ti melt component with different Ti:Fe,Mg ratios, the silicate portion of the composition shifts to different olivine normative compositions (Fig. 7). Compositions with higher TiO_2^* contents have the largest change in 'normative olivine' because they are closer to the Fe,Mg–Ti apex of the compositional tetrahedron (Fig. 7). Using this projection scheme, we see the MSPs of the high-Ti compositions studied in graphite capsule experiments form a trend in this projection space; where higher pressure MSPs display more olivine normative compositions (Fig. 8).

In the previous section we have shown that the Fe–Mg systematics of olivine–melt is accounted for by the complexing of Fe^{2+}–Ti^{3+}–Ti^{4+} and possibly Mg^{2+} in the melt. Ti^{3+} can also account for the shifts in olivine–opx MSP. A possible substitution mechanism for incorporating Ti^{3+} into an Fe,Mg–Ti melt component is by reduction of Ti^{4+} already in the complex, and therefore ejecting an Fe or Mg from the complex by charge balance. The substitution mechanism is similar to a Al-Tschermak substitution as follows:

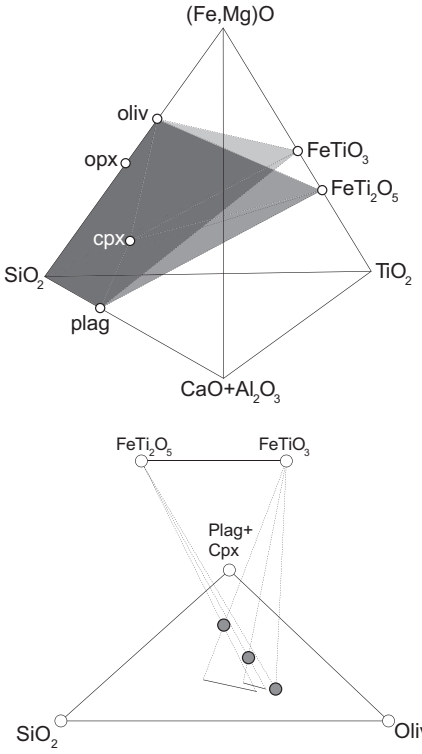

Fig. 7. Adapted projection scheme of Longhi et al. (1974). By projecting through different (Fe,Mg)–Ti melt components we can see the apparent effect on the composition. Lowering f_{O_2} would move the (Fe,Mg)–Ti melt component toward the TiO_2 end member by introducing more Ti^{3+}. Three schematic liquid compositions are shown with varying amounts of $FeO + MgO + TiO_2$.

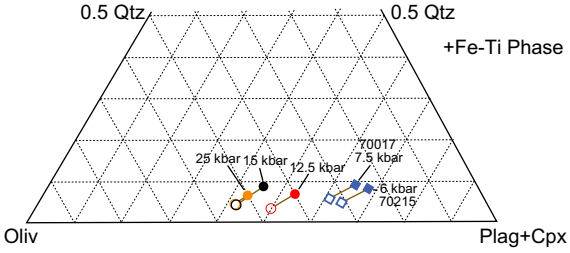

Fig. 8. Enlarged portion of the Plag + Cpx–Olivine–Quartz psuedo-ternary diagram. Filled symbols are compositions that have had their MSP's experimentally determined in graphite capsules. There is a trend that more olivine normative compositions have higher MSP's. Filled symbols are projected through $(Fe,Mg)TiO_3$ and open circles are projected through $(Fe,Mg)Ti_2O_5$. The $(Fe,Mg)Ti_2O_5$ projection is more 'reducing' assuming that Ti^{3+} is substituting into the Fe–Ti melt component by Eq. (4) and therefore appropriate for shifts in the phase boundaries for experiments in Fe-capsules.

$$\begin{aligned}&(Fe,Mg)Ti_2O_{5(cplx)} \\ &\quad + 2x(Ti^{4+})_{(cplx)} \Longleftrightarrow (Fe,Mg)_{1-x}Ti_{2+x}O_{5(cplx)} \\ &\quad + 2x(Ti^{3+})_{(cplx)} + x(Fe^{2+},Mg)_{(melt)} \end{aligned} \quad (4)$$

Here 'cplx' refers to the Fe–Ti complex in the melt that olivine cannot exchange with, while $(Fe^{2+},Mg)_{melt}$ is then available to be incorporated into olivine. The armalcolite stoichiometry of the complex is meant to be general and not a specific melt component.

Assuming that the (Fe,Mg)–Ti melt component used to project through is related to the actual (Fe,Mg)–Ti component of the melt, then according to Eq. (4) we must project through a composition closer to TiO_2 on the (Fe,Mg)O–TiO_2 join for reduced systems. Projecting through a more Ti-rich melt complex indeed shifts the melt compositions to more olivine normative compositions, despite the overall bulk composition being the same. The more olivine normative nature of the bulk system at low f_{O_2} is consistent with olivine being stable at higher pressures.

Our experiments show that under reducing conditions the MSPs move to higher pressures. A composition with a Ti-rich liquid (i.e. the A15R glass) would have the largest change in 'normative olivine' because it is closest to the Fe,Mg–Ti apex of the tetrahedron, consistent with our experimental data (Fig. 5). By shifting the projected (Fe,Mg)–Ti melt component towards the TiO_2 apex and reprojecting through this component, the compositions become more olivine normative, and their shift is proportional to the increase in the multiple saturation pressure for the orange and red glasses.

5. SIGNIFICANCE FOR THE PETROGENESIS OF HIGH-TITANIUM LIQUIDS

The determination of the pressure of origin for these high-Ti lavas is critical for understanding the distribution of dense ilmenite rich cumulates within the Moon. Melting of these cumulates produces high density liquids. The high densities of these liquids have led many to investigate their compressibility (Delano, 1990; Circone and Agee, 1996; Sakamaki et al., 2010; van Kan Parker et al., 2011) and to speculate on their eruptability (Hess, 1991; Tanton et al., 2002). With our experimental determination of the depth of origin we can evaluate these models.

The oxidation state of the high-Ti source region has been studied for the A17O glass, and estimates vary between ΔIW+1 to ΔIW−2 with the best estimate of ΔIW−0.6 (Sato, 1979; Weitz et al., 1997; Nicholis and Rutherford, 2009). The best estimate for the orange glass f_{O_2} thus falls in the range of our experimental end members of ΔIW+1.3 and ΔIW−2.1. Linear interpolation of the MSP between our two end members gives our best estimate for the depth of origin for the A17O glass (Fig. 5).

We have calculated the compressibility curves for the A17O liquid following the methods of Delano (1990) and Lange and Carmichael (1987) using the zero pressure liquidus temperature of the orange glass and a $K'_T = 6$, (Fig. 9).

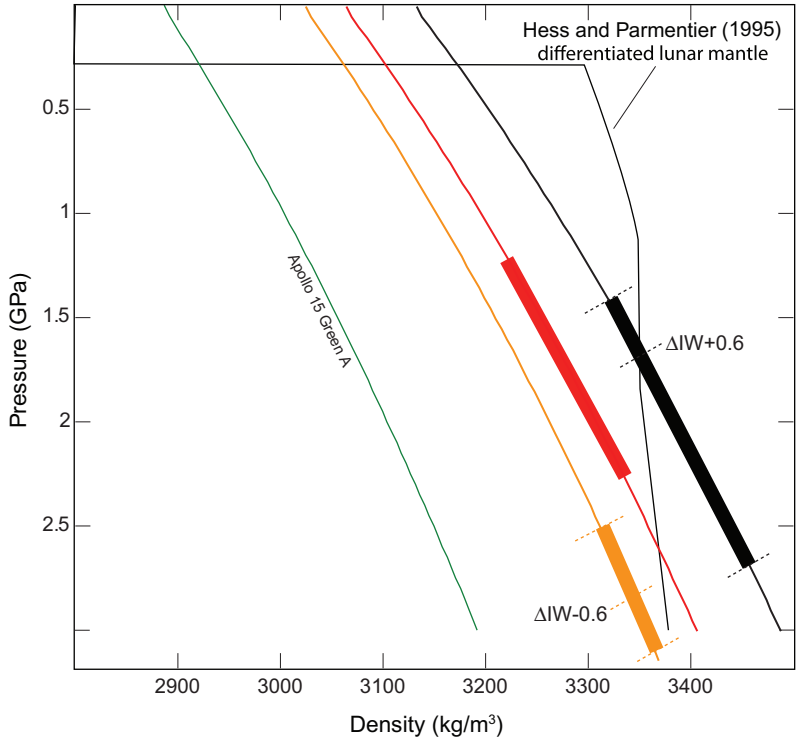

Fig. 9. Calculated liquid density–depth curves. We use the molar volumes from Lange and Carmichael (1987) to produce the zero pressure estimates of density of the liquid, and the method of Delano (1990) to calculate the high pressure densities assuming an intermediate value of 6 for K'. The density of the lunar mantle after cumulate overturn is shown from Hess and Parmentier (1995). The colored curves are for the A17O (orange), A15R (red), A14B (black), and Apollo 15 group A glasses (green). The ranges of MSP for the high-Ti glasses are shown as thick bars. The high pressure end of the range of black glass MSP is extrapolated to ΔIW−2.1. (For interpretation of the references to color in this figure legend, the reader is referred to the web version of this article.)

In Fig. 9 the shallow MSP from graphite capsule experiments and the deep MSP from Fe-metal capsule experiments is highlighted as bolder part of the compressibility curve. Over the entire range we explored, and at our best guess at 2.8 GPa, our best estimate for the pressure of origin for the orange glass, the orange glass is buoyant with respect to a model differentiated lunar mantle composition (Hess and Parmentier, 1995). Our calculated density is in agreement with the recent experimental study of the compressibility of the orange glass (van Kan Parker et al., 2011).

Unfortunately, there is no estimate for the source region f_{O_2} of the A15R glass, however most lunar materials fall into a relatively narrow range of f_{O_2} between $\Delta IW-2$ to $\Delta IW = 0$ (Sato et al., 1973; Haggerty, 1978). The range in experimental MSP's for the A15R glass is from 1.3 to 2.2 GPa, and it is notable that these pressures are at least 0.6 GPa lower ($\sim$ 120 km shallower) than the MSP of the

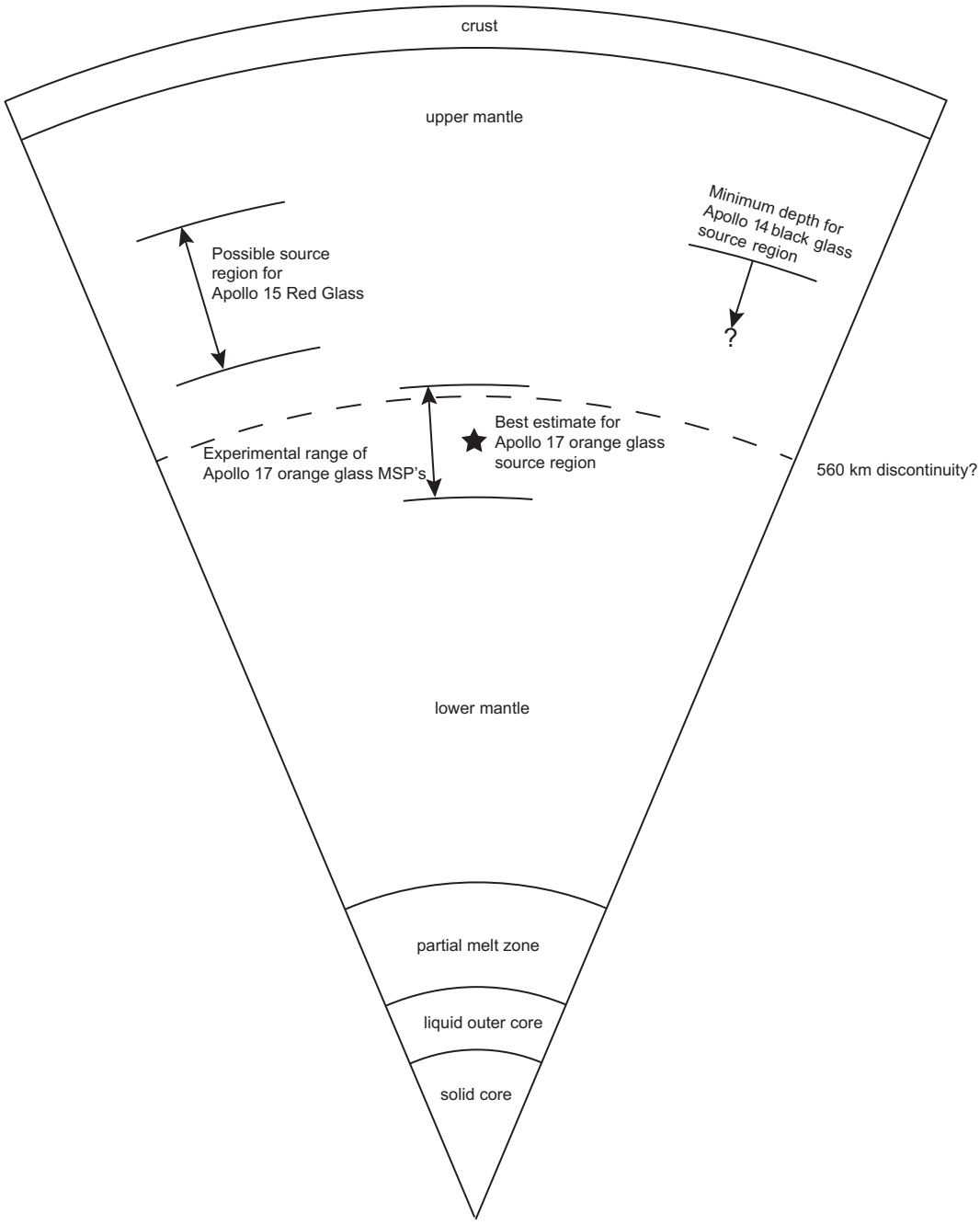

Fig. 10. Cross-section of the lunar interior based on the internal structure from Wieczorek (2009) and Weber et al. (2011). The distribution of the source regions for the A15R, A17O, and Apollo 14 black glass are shown. Minimum depths are based on experiments at IW+1.2 and maximum depths are based on experiments at IW−2.1, and the star shows the best estimate for the A17O depth of origin based on its measured intrinsic f_{O_2} of IW−0.6. The depths are based on the pressure gradient from Baumgardner and Anderson (1981).

A17O glass. The calculated densities of the A15R glass suggests that like the A17O glass it is buoyant over the entire range of f_{O_2} explored here (Fig. 9).

The density and compressibility of the A14B glass has been theoretically (Delano, 1990) and experimentally (Circone and Agee, 1996; Sakamaki et al., 2010) determined to be buoyant with respect to a residual mantle at the depth of its graphite capsule MSP. However when considering the effect that f_{O_2} has on the MSP of the black glass, the highly compressible A14B glass is *only* buoyant at the high end of the f_{O_2} range. Using the fact that the projection of the A14B composition at reducing conditions overlaps the projection A17O (Fig. 8) we predict that the MSP of the A14B in Fe-metal capsules would be similar to that of the A17O. Linear interpolation between the experimental ΔIW+1.3 MSP at 1.5 GPa (Wagner and Grove, 1997), and inferred ΔIW−2.1 MSP constrains the black glass source region f_{O_2} at >ΔIW+0.6 in order for it to be buoyant with respect to the differentiated mantle density line of Hess and Parmentier (1995) (Fig. 9). We thus suggest that its source region is more oxidizing than the orange glass source region.

It is clear that the oxygen fugacity of the source region must be taken into account in determining the depth of origin for any high-Ti magma. Using this new and internally consistent data set it is apparent that the MSP's for high-Ti glasses span a range of pressures from 1.3 GPa up to 2.8 GPa. These values correspond to a depth interval of 250–640 km in the Moon (Baumgardner and Anderson, 1981). The distribution of the source material for these glasses is thus spread over a large portion of the lunar mantle (Fig. 10). The variability in the depth of high-titanium magma source regions is evidence that both overturn and convective mixing of magma ocean cumulates was inefficient at segregating all of the high-Ti source material to a single depth. It is likely that the lunar mantle is quite heterogeneous on a horizontal basis, as well as a vertical basis (Ringwood and Kesson, 1976; Hess and Parmentier, 1995; Tanton et al., 2002).

ACKNOWLEDGMENTS

This research was supported by NASA Grant NNG06G167G to T.L.G. The authors thank M. Rutherford, D. Canil, W. Van Westrenen, and an anonymous reviewer for constructive feedback on this and a previous version of the manuscript. We also thank R. Korotev for editorial handling and review. The authors also would like to thank N. Chaterjee for microprobe assistance and E. Medard, B. Charlier and J. Barr for helpful discussions.

REFERENCES

Armstrong J. T. (1995) CITZAF—a package of correction programs for the quantitative electron microbeam X-ray-analysis of thick polished materials, thin-films, and particles. *Microbeam Anal.* **4**, 177–200.

Ballhaus C., Berry R. F. and Green D. H. (1991a) Erratum. *Contrib. Mineral. Petrol.* **108**, 384.

Ballhaus C., Berry R. F. and Green D. H. (1991b) High pressure experimental calibration of the olivine–orthopyroxene–spinel oxygen geobarometer: implications for the oxidation state of the upper mantle. *Contrib. Mineral. Petrol.* **107**, 27–40.

Baumgardner J. R. and Anderson O. L. (1981) Using the thermal pressure to compute the physical properties of terrestrial planets. *Adv. Space Res.* **1**, 159–176.

Boyd F. R. and England J. L. (1960) Apparatus for phase-equilibrium measurements at pressures up to 50 kilobars and temperatures up to 1750 °C. *J. Geophys. Res.* **65**, 741–748.

Canil D. and Bellis A. J. (2008) Phase equilibria in a volatile-free kimberlite at 0.1 MPa and the search for primary kimberlite magma. *Lithos* **105**, 111–117.

Circone S. and Agee C. B. (1996) Compressibility of molten high-Ti mare glass: evidence for crystal–liquid density inversions in the lunar mantle. *Geochim. Cosmochim. Acta* **60**, 2709–2720.

Colson R. O., McKay G. A. and Taylor L. A. (1988) Temperature and composition dependencies of trace element partitioning—olivine/melt and low-Ca pyroxene/melt. *Geochim. Cosmochim. Acta* **52**, 539–553.

Delano J. W. (1980) Chemistry and liquidus phase relations of Apollo 15 red glass: implications for the deep lunar interior. *Lunar Planet. Sci. Conf. Proc.* **11**, 251–288.

Delano J. W. (1986) Pristine lunar glasses—criteria, data, and implications. *J. Geophys. Res.* **91**, D201–D213.

Delano J. W. (1990) Buoyancy-driven melt segregation in the earth's moon: I. Numerical results. *Lunar Planet. Sci. Conf. Proc.* **20**, 3–12.

Dickinson, Jr., J. E. and Hess P. C. (1985) Rutile solubility and titanium coordination in silicate melts. *Geochim. Cosmochim. Acta* **49**, 2289–2296.

Elkins-Tanton L. T., Chatterjee N. and Grove T. L. (2003) Experimental and petrological constraints on lunar differentiation from the Apollo 15 green picritic glasses. *Meteorit. Planet. Sci.* **38**, 515–527.

Elkins Tanton L. T., Van Orman J. A., Hager B. H. and Grove T. L. (2002) Re-examination of the lunar magma ocean cumulate overturn hypothesis: melting or mixing is required. *Earth Planet. Sci. Lett.* **196**, 239–249.

Filiberto J. and Dasgupta R. (2011) Fe^{2+}–Mg partitioning between olivine and basaltic melts: applications to genesis of olivine–phyric shergottites and conditions of melting in the Martian interior. *Earth Planet. Sci. Lett.* **304**, 527–537.

Gaetani G. A., Asimow P. D. and Stolper E. M. (2008) A model for rutile saturation in silicate melts with applications to eclogite partial melting in subduction zones and mantle plumes. *Earth Planet. Sci. Lett.* **272**, 720–729.

Green D. H., Ringwood A. E., Hibberson W. O. and Ware N. G. (1975) Experimental petrology of Apollo 17 mare basalts. *Lunar Planet. Sci. Conf. Proc.* **6**, 871–893.

Grove T. L. (1981) Use of FePt alloys to eliminate the iron loss problem in 1-atmosphere gas mixing experiments—theoretical and practical considerations. *Contrib. Mineral. Petrol.* **78**, 298–304.

Haggerty S. E. (1978) The redox state of planetary basalts. *Geophys. Res. Lett.* **5**, 443–446.

Hays J. F. (1966) Stability and properties of synthetic pyroxene $CaAl_2SiO_6$. *Am. Mineral.* **51**, 1524–1529.

Hess P. C. (1991) Diapirism and the origin of high TiO_2 mare glasses. *Geophys. Res. Lett.* **18**, 2069–2072.

Hess P. C. and Parmentier E. M. (1995) A model for the thermal and chemical evolution of the Moon's interior: implications for the onset of mare volcanism. *Earth Planet. Sci. Lett.* **134**, 501–514.

Holloway J. R., Pan V. and Gudmundsson G. (1992) High-pressure fluid-absent melting experiments in the presence of graphite—oxygen fugacity, ferric ferrous ratio and dissolved CO_2. *Eur. J. Mineral.* **4**, 105–114.

Jones J. H. (1988) Partitioning of Mg and Fe between olivine and liquids of lunar compositions: the roles of composition,

pressure and Ti speciation. *Lunar Planet. Sci. Conf. Abstr.* **19**, 561–562.

Kessel R., Beckett J. and Stolper E. (2003) Experimental determination of the activity of chromite in multicomponent spinels. *Geochim. Cosmochim. Acta* **67**, 3033–3044.

Kesson S. E. and Lindsley D. H. (1975) The effects of Al^{3+}, Cr^{3+}, and Ti^{3+} on the stability of armalcolite. *Lunar Planet. Sci. Conf. Proc.* **6**, 911–920.

Kress V. C. and Carmichael I. S. E. (1991) The compressibility of silicate liquids containing Fe_2O_3 and the effect of composition, temperature, oxygen fugacity and pressure on their redox states. *Contrib. Mineral. Petrol.* **108**, 82–92.

Kushiro I. and Mysen B. O. (2002) A possible effect of melt structure on the Mg–Fe^{2+} partitioning between olivine and melt. *Geochim. Cosmochim. Acta* **66**, 2267–2272.

Lange R. A. and Carmichael I. S. E. (1987) Densities of Na_2O–K_2O–MgO–FeO–Fe_2O_3–Al_2O_3–TiO_2–SiO_2 liquids: new measurements and derived partial molar properties. *Geochim. Cosmochim. Acta* **51**, 2931–2946.

Lindsley D. H. and Dixon S. A. (1976) Diopside–enstatite equilibria at 850 degrees to 1400 degrees C, 5 to 35 kb. *Am. J. Sci.* **276**, 1285–1301.

Longhi J. (2005) Temporal stability and pressure calibration of barium carbonate and talc/pyrex pressure media in a piston–cylinder apparatus. *Am. Mineral.* **90**, 206–218.

Longhi J., Walker D., Grove T. L., Stolper E. M. and Hays J. F. (1974) The petrology of the Apollo 17 mare basalts. *Lunar Planet. Sci. Conf. Proc.* **5**, 447–469.

Longhi J., Walker D. and Hays J. F. (1972) Petrography and crystallization history of basalts 14310 and 14072. *Lunar Planet. Sci. Conf. Proc.* **3**, 131–139.

Longhi J., Walker D. and Hays J. F. (1978) The distribution of Fe and Mg between olivine and lunar basaltic liquids. *Geochim. Cosmochim. Acta* **42**, 1545–1558.

Medard E., McCammon C. A., Barr J. A. and Grove T. L. (2008) Oxygen fugacity, temperature reproducibility, and H_2O contents of nominally anhydrous piston–cylinder experiments using graphite capsules. *Am. Mineral.* **93**, 1838–1844.

Mysen B. (2007) Partitioning of calcium, magnesium, and transition metals between olivine and melt governed by the structure of the silicate melt at ambient pressure. *Am. Mineral.* **92**, 844–862.

Mysen B. and Neuville D. (1995) Effect of temperature and TiO_2 content on the structure of $Na_2Si_2O_5$–$Na_2Ti_2O_5$ melts and glasses. *Geochim. Cosmochim. Acta* **59**, 325–342.

Mysen B. O. (2006) Redox equilibria of iron and silicate melt structure: implications for olivine/melt element partitioning. *Geochim. Cosmochim. Acta* **70**, 3121–3138.

Nicholis M. G. and Rutherford M. J. (2009) Graphite oxidation in the Apollo 17 orange glass magma: Implications for the generation of a lunar volcanic gas phase. *Geochim. Cosmochim. Acta* **73**, 5905–5917.

Papike J. J., Ryder G., Shearer C. K. (1998) Lunar samples. In *Planetary Materials*, vol. 36 of Reviews in Mineralogy. Mineralogical Society of America, 1015 Eighteenth St., NW, Suite 601, Washington, DC 20036, pp. E1–E234.

Press W. H., Flannery B. P., Teukolsky S. A. and Vetterling W. T. (1986) *Numerical Recipes: The Art of Scientific Computing*. Cambridge University Press.

Putirka K., Johnson M., Kinzler R., Longhi J. and Walker D. (1996) Thermobarometry of mafic igneous rocks based on clinopyroxene–liquid equilibria, 0–30 kbar. *Contrib. Mineral. Petrol.* **123**, 92–108.

Ringwood A. E. and Kesson S. E. (1976) A dynamic model for mare basalt petrogenesis. *Lunar Planet. Sci. Conf. Proc.* **7**, 1697–1722.

Roeder P. L. and Emslie R. F. (1970) Olivine–liquid equilibrium. *Contrib. Mineral. Petrol.* **29**, 275–289.

Sakamaki T., Ohtani E., Urakawa S., Suzuki A., Katayama Y. and Zhao D. (2010) Density of high-Ti basalt magma at high pressure and origin of heterogeneities in the lunar mantle. *Earth Planet. Sci. Lett.* **299**, 285–289.

Sato M. (1979) The driving mechanism of lunar pyroclastic eruptions inferred from the oxygen fugacity behavior of Apollo 17 orange glass. *Lunar Planet. Sci. Conf. Proc.* **10**, 311–325.

Sato M., Hickling N. L. and McLane J. E. (1973) Oxygen fugacity values of Apollo 12, 14, and 15 lunar samples and reduced state of lunar magmas. *Lunar Planet. Sci. Conf. Proc.* **4**, 1061–1079.

Snyder G. A., Taylor L. A. and Neal C. R. (1992) A chemical model for generating the sources of mare basalts—combined equilibrium and fractional crystallization of the lunar magmasphere. *Geochim. Cosmochim. Acta* **56**, 3809–3823.

Solomon S. C. and Longhi J. (1977) Magma oceanography: I. Thermal evolution. *Lunar Planet. Sci. Conf. Proc.* **8**, 583–599.

Toplis M. J. (2005) The thermodynamics of iron and magnesium partitioning between olivine and liquid: criteria for assessing and predicting equilibrium in natural and experimental systems. *Contrib. Mineral. Petrol.* **149**, 22–39.

Ulmer P. and Luth R. W. (1991) The graphite–COH fluid equilibrium in P, T, f_{O_2} space. *Contrib. Mineral. Petrol.* **106**, 265–272.

van Kan Parker M., Agee C. B., Duncan M. S. and van Westrenen W. (2011) Compressibility of molten apollo 17 orange glass and implications for density crossovers in the lunar mantle. *Geochim. Cosmochim. Acta* **75**, 1161–1172.

Wagner T. P. and Grove T. L. (1997) Experimental constraints on the origin of lunar high-Ti ultramafic glasses. *Geochim. Cosmochim. Acta* **61**, 1315–1327.

Warren P. H. (1985) The magma ocean concept and lunar evolution. *Annu. Rev. Earth Planet. Sci.* **13**, 201–240.

Weber R. C., Lin P. Y., Garnero E. J., Williams Q. and Lognonné P. (2011) Seismic detection of the lunar core. *Science* **331**, 309.

Weitz C. M., Rutherford M. J. and Head, III, J. W. (1997) Oxidation states and ascent history of the Apollo 17 volcanic beads as inferred from metal–glass equilibria. *Geochim. Cosmochim. Acta* **61**, 2765–2775.

Wieczorek M. A. (2009) The interior structure of the moon: what does geophysics have to say? *Elements* **5**, 35–40.

Xirouchakis D., Hirschmann M. M. and Simpson J. A. (2001) The effect of titanium on the silica content and on mineral–liquid partitioning of mantle-equilibrated melts. *Geochim. Cosmochim. Acta* **65**, 2201–2217.

Yasuda A. and Fujii T. (1993) Application of a solid-electrolyte oxygen fugacity sensor to high-pressure experiments. *Phys. Earth Planet. In.* **80**, 49–64.

Associate editor: Randy L. Korotev